Quinary structure kinetically controls protein function and dysfunction

Tarique Khan[1,3], Tejbir S. Kandola[1,3], Jianzheng Wu[1,2,3], Ellen Ketter[1,3], Shriram Venkatesan[1], Jeffrey J. Lange[1], Alejandro Rodriguez Gama[1], Andrew Box[1], Jay R. Unruh[1], Malcolm Cook[1], and Randal Halfmann[1,2,]*

[1] Stowers Institute for Medical Research, 1000 East 50th Street, Kansas City, MO 64110
[2] Department of Molecular and Integrative Physiology, University of Kansas Medical Center, 3901 Rainbow Boulevard, Kansas City, KS 66160, USA
[3] These authors contributed equally
*Corresponding author: rhn@stowers.org

Highlights

- Quinary structure enables switch-like regulation of protein activity
- Distributed Amphifluoric FRET parameterizes quinary assembly in living cells
- Condensation drives physiological and proteotoxic activities of low complexity “prion-like” sequences
- Nucleation-limited structured assembly drives prion behavior

Summary

Protein self-assemblies compartmentalize cellular biochemistry and encode molecular memories; but, they also precipitate incurable degenerative diseases. These activities involve vastly different structures and time scales. Recognizing the dominant role of nucleation in self-assembly kinetics, we hypothesized that quinary structures function, in part, by dictating the energy barrier of nucleation. To investigate, we developed Distributed Amphifluoric FRET (DAmFRET), an approach to characterize protein nucleation in living cells. DAmFRET exploits a photoconvertible fluorophore and heterogeneous levels of expression to quantify a protein’s self-assembly as a function of its concentration in living cells. Using DAmFRET, we characterize dozens of self-assembling proteins, and find that structural complexity produces nucleation barriers that kinetically control the proteins’ cellular activities. Pathological “prion-like” proteins tended to form metastable condensates, whereas prions with physiological functions did not. Our results suggest that quinary structure broadly distinguishes the kinetics of subcellular organization, signal propagation, cytoplasmic inheritance, and proteotoxicity.

Keywords: prions, proteopathy, aggregation, inflammation, signaling, nucleation, phase separation, amyloid, quinary

INTRODUCTION

Protein structure dictates function. Some functions, however, emerge only from contiguous assemblies of proteins that defy conventional notions of structure. These comprise a fifth, or *quinary*, level of protein structure (beyond primary, secondary, tertiary, and quaternary) that is most succinctly defined by an absence of stoichiometry (Edelstein, 1980; Riback et al., 2017; Vaĭnshteĭn, 1973; Wallace et al., 2015).

Quinary assemblies compartmentalize cellular biochemistry, amplify signals, regulate the flow of macromolecules and genetic information, and record aspects of cellular history (Banani et al., 2017; Caudron and Barral, 2013; Chakrabortee et al., 2016a; Halfmann, 2016; Si and Kandel, 2016; Wu and Fuxreiter, 2016). They can also be dysfunctional, as for degenerative diseases like Alzheimer's, Parkinson's, and ALS (Knowles et al., 2014).

Quinary assemblies range from disordered dynamic liquid droplets to crystalline arrays of globular protein subunits (Edelstein, 1980; Lyle et al., 2002; Vaĭnshteĭn, 1973). Each polypeptide within a quinary assembly engages others across multiple distinct (with one exception as described below), low-affinity interfaces. One consequence of this is that quinary structure can be extraordinarily cooperative and even *critically* sensitive to protein concentration (Zhao and Moore, 2003). Another consequence is that the nucleation, or birth, of a new assembly is inherently probabilistic on the nanoscopic scale. The nucleation barrier determines the extent of that improbability, and therefore how long, on average, a supersaturated system of proteins remains dispersed or unstructured at a given concentration. The more intricate (or improbable) the molecular fluctuations in density and conformation required to form the first embryo of quinary structure, the larger the nucleation barrier (Vekilov, 2012). Because nucleation by definition is rate-limiting for assembly, the magnitude of the nucleation barrier determines the spatial and temporal scales of quinary protein dynamics. Although these concepts have been well established in polymer physics and structural biology (Michaels et al., 2017; Vekilov, 2012; ten Wolde and Frenkel, 1997), their implications for protein regulation are heretofore unexplored. Does nature exploit nucleation barriers to compartmentalize protein activity in space and time?

The existence of remarkable epigenetic elements known as prions (Halfmann and Lindquist, 2010) suggests that, in principle, it does. Prion-forming proteins normally exist as dispersed monomers. But this state is only kinetically stable: given enough time it will inevitably give way to a thermodynamically-favored, assembled state (Glover et al., 1997; Tanaka et al., 2006). That assembly -- the prion -- takes the form of an exquisitely ordered quasi-two-dimensional polymer (Kashchiev, 2015; Nelson et al., 2005; Tycko and Wickner, 2013; Wasmer et al., 2008; Wu and Fuxreiter, 2016; Zhang and Schmit, 2016; Zhao and Moore, 2003). It arises so infrequently that multiple generations of cells may pass without its appearance. However, specific interactions with signaling molecules (Cai et al., 2014; Daskalov et al., 2015a; Garcia et al., 2016) or perturbations to protein homeostasis (Doronina et al., 2015; Suzuki et al., 2012; Tyedmers et al., 2008) can dramatically increase prion nucleation. Once nucleated, the prion perpetuates until almost all of the prion protein in the cell has assembled into the same form (Cheng et al., 2010; Satpute-Krishnan and Serio, 2005; Tanaka et al., 2006). Should a fragment of the prion then find its way into a naive pool of the proteins within a foreign cell or organism, it assembles those proteins as well. This capability grants prions properties otherwise found only in nucleic acids -- the ability to transmit phenotypes between organisms and across generations.

Prions reveal that extremes of quinary structure coincide with extremes of kinetic control. But does quinary structure broadly *function* to regulate protein activity kinetics?

We developed a system based on cytometry and homotypic FRET to rapidly assess nucleation barriers to self-assembly of a target protein *in vivo*. The system was applied to dozens of functionally diverse proteins, revealing a relationship between the complexity of a quinary structure and its nucleation barrier that governs the spatial and temporal scale of its biological activities: disordered assemblies exhibited negligible nucleation barriers whereas ordered assemblies exhibited nucleation barriers that precluded their assembly over cellular timescales. The former exerted intracellular functions; the latter exerted multicellular functions. Kinetically frustrated assemblies produced proteotoxicity. Hence, quinary structures impose nucleation barriers that broadly govern protein function and dysfunction.

RESULTS

Distributed Amphifluoric FRET (DAmFRET) distinguishes quinary assembly mechanisms

If quinary structure indeed functions to exert switch-like kinetic control, then we should not expect to observe it under most physiological conditions. How then can we unmask, systematically, the quinary structural preferences of proteins?

The probabilistic nature of nucleation means that any quinary structure that is rate-limited by nucleation must inevitably occur, given enough time. That length of time may not be practical experimentally. Quantifying rare nucleation events over experimental time scales therefore necessitates the examination of very large numbers of independent molecular systems.

Droplet microfluidics offers one approach to observing nucleation (Michaels et al., 2017). However, it necessarily divorces proteins from intracellular factors that shape their folding tendencies. Living cells offer another approach.

We therefore sought a reporter system for protein self-assembly in the single cell which could be assessed in large populations of independent cells expressing the protein over a range of concentrations, so as to yield a concentration-dependent, conditional distribution of self-assembly corresponding to the energetics of nucleation (Michaels et al., 2017). The system would have to: provide single-cell readouts; scale to report on thousands of cells in a population; ensure independence between cells; be manipulable to produce expression over a wide concentration range; provide a sensitive readout of protein expression and cytosolic volume (as required for determining concentration); and work equally well across dozens of different target proteins.

The necessity to acquire single-cell measurements across large cell populations suggested flow cytometry as the appropriate platform. The need to determine cytosolic volume and to evaluate protein localization within each cell further led us to imaging flow cytometry (Basiji and O'Gorman, 2015).

Ensuring experimental independence of each cell required that we restrict intercellular interactions. We therefore employed the unicellular eukaryote, budding yeast. Notably, yeast cell walls are impermeable to extracellular amyloids and prion-containing exosomes (Kabani and Melki, 2015; King and Diaz-Avalos, 2004) whereas cultured mammalian cells readily internalize these structures (Grassmann et al., 2013). We eliminated the additional possibility of mitotic inheritance of nucleated assemblies by genetically inducing cell cycle arrest during query protein expression (see Methods). In short, every cell of the resulting yeast strain can be considered as an independent, nanoliter-volume, protein-assembly vessel.

Many techniques were considered for the reporter. Förster Resonance Energy Transfer (FRET), which occurs between two fluorophores having overlapping spectra when they are brought in close proximity, is widely used to detect interactions between two corresponding protein species fused to those fluorophores (Jares-Erijman and Jovin, 2003). However, creating the two fusions for each protein, and expressing them to the same ratio in all cells across a range of expression levels, would be exceedingly difficult. We likewise excluded protein complementation and two hybrid assays from consideration. Available approaches that use a single fusion protein to detect self-assembly, such as fluorescence anisotropy and enzyme loss of function assays, were not considered due to their limited dynamic range and throughput.

We reasoned that high-throughput, sensitized emission FRET between complementary fluorophores could be realized if they were both expressed from the same genetic construct. Individual molecules of the fusion protein would have to mature stochastically into one or the other fluorophore, resulting in a mixture of the two at the cellular level. In this way, a consistent ratio of donor to acceptor molecules could be produced regardless of the protein's expression level. We further reasoned that photoconvertible fluorescent proteins could be employed for this purpose. After testing several, we chose to proceed with mEos3.1, a monomeric bright green fluorescent protein that can be converted irreversibly to a bright red fluorescent form upon illumination with violet light (Zhang et al., 2012). Importantly, the emission spectrum of the green form strongly overlaps the excitation spectrum of the red form, as necessary for FRET to occur (Fig. 1A). The ratio of green to red molecules and thereby the sensitivity of the mixture to quinary structure can be precisely controlled by modulating the intensity and duration of violet light exposure. We term this approach Amphifluoric FRET (AmFRET) due to the dual nature of the fluorescent moiety.

To assess quinary assembly as a function of concentration, we needed to evaluate the distribution of AmFRET values, or DAmFRET, across a wide range of intracellular protein concentrations (Fig. 1C). We therefore inducibly expressed mEos3.1 fusion proteins from an episomal plasmid whose copy number varies by approximately one hundred fold between cells (Fig. 1B; Futcher and Cox, 1984; Loison et al., 1989). After eighteen hours of protein expression, cell cultures were uniformly illuminated with violet light to convert a fraction of mEos3.1 molecules from the green (donor) to the red (acceptor) form. We limited the illumination to an empirically optimized dose that yielded maximum FRET intensity. We established that photoconversion efficiency was insensitive to expression level as well as to the identity and structure of the fusion partner (Fig. S1B), enabling us to indirectly measure total protein levels as the product of intensity of acceptor fluorescence and an empirically determined molecular brightness and photoconversion factor (see Methods). Each cell's total protein level was then divided by its approximate cytosolic volume as calculated from the bright-field image to derive absolute protein concentrations. We used the ratio of acceptor fluorescence when excited indirectly (at 488 nm) to directly (at 561 nm) to approximate FRET efficiency, and hereafter refer to this ratio as simply, “AmFRET”.

To validate the DAmFRET approach, we fused mEos3.1 to proteins of diverse known self-assembling tendencies (Fig. 1D): SPOP, hnRNPA1, and p28. SPOP is a human nuclear speckle protein that assembles through a single interface into truly one-dimensional polymers (Marzahn et al., 2016). Because nucleation requires more than one dimension of order, these are non-nucleated quinary structures (Kashchiev, 2015; Zhao and Moore, 2003). hnRNPA1 is a human RNA-binding protein that condenses into internally disordered assemblies upon exposure to physiological stresses (Molliex et al., 2015). Finally, the turnip crinkle virus replication protein, p28, nucleates a single large assembly in each infected cell that functions to privatize the virus' RNA-dependent RNA polymerase activity to a single genomic ssRNA (Zhang et al., 2017).

When expressed in yeast, mEos3.1 without a fusion partner produced negligible AmFRET even at the highest concentrations measured -- approximately 300 μM (Fig. 1E). In contrast, cells expressing SPOP exhibited AmFRET that gently increased with concentration. Cells expressing hnRNPA1 produced a similar distribution, albeit with a steeper concentration dependence, as expected for cooperative assembly (Zhao and Moore, 2003). Finally, cells expressing p28 lacked AmFRET at low concentrations but then sharply acquired AmFRET at an apparent critical concentration of 13 μM. Such a sudden transition in material property is the hallmark of a phase boundary, in this case between fully dispersed monomers and nucleated self-assemblies.

Quinary structure can kinetically control protein function

Having validated DAmFRET for protein assemblies with small to nonexistent nucleation barriers, we next investigated quinary proteins whose functions appear to be governed by large nucleation barriers. Multiple proteins have recently been discovered to fulfill their cellular functions through a switch-like transition from dispersed monomers to self-sustaining polymers.

We focused initially on ASC, the core scaffolding protein of mammalian inflammasomes. The nucleation of ASC into a right-handed triple helical polymer confers a digital, all-or-none responsiveness to inflammatory stimuli (Cai et al., 2014; Cheng et al., 2010; Lu et al., 2014). When characterized by DAmFRET, ASC produced a distribution unlike those of thermodynamically-controlled oligomeric and higher-order assemblies. At low concentrations, all cells lacked AmFRET. But at higher concentrations, a second population emerged with intense AmFRET (Fig. 2A). The two populations were discontinuous yet overlapped on the abscissa, resulting in a strongly bimodal distribution at intermediate concentrations. This bimodality indicates that the two states of the protein are mutually exclusive and the presence of one or the other is not determined solely by concentration on the time scale of our experiment.

These data lead to the following two predictions. First, nucleation of the AmFRET-positive state of ASC is so infrequent that, on average, it will occur only once per cell. Absent secondary processes like fragmentation, this must result in a single fluorescent punctum. An analysis of the imaging data revealed that most cells in the top population indeed contained a single intensely fluorescent punctum (Fig. S2A and Methods). Cells in the bottom population contained fully dispersed fluorescence. Second, the absence of cells with intermediate values of AmFRET indicates that the single nucleus grows so rapidly as to achieve steady state near instantaneously. To evaluate, we recorded the expression level and distribution of ASC over time in multiple individual yeast cells. We found that fluorescence accumulated to high levels in a fully diffuse state. But then, in a stochastic fashion for each cell, it collapsed near-instantaneously into discrete puncta (Movie S2 and Fig. 2B). These kinetics and puncta morphology closely resemble ASC activation in human cells (Cheng et al., 2010).

We next asked if other polymeric signaling proteins similarly transition semistochastically from monomers to fully assembled states when deeply supersaturated. We evaluated three such proteins: the CARD domain of MAVS, an innate immune signaling protein in the same superfamily as ASC, but with an opposite helical symmetry in the assembled state (Wu et al., 2014; Xu et al., 2015); the prion-forming domain (PrD) of HET-s, a functional prion protein from the filamentous fungus *Podospora anserina* with a structure completely unlike that of ASC and MAVS; and finally, the putative PrD of sesA, another unrelated signaling protein implicated by genetic and bioinformatic evidence as a prion in the filamentous fungus, *Nectria haematococca* (Daskalov et al., 2012). As for ASC, all three of these proteins produced highly bimodal distributions of AmFRET (Fig. 2C). Well-characterized mutations in the subunit interface of MAVS CARD (Cai et al., 2014) each prevented the AmFRET-positive population (E26A is shown; R41A, R64A, and R65A produced the same effect and are not shown), confirming that it corresponds with the acquisition of native-like CARD assemblies.

Physiological activation of ASC, MAVS, and HET-s occurs through interactions of each protein with oligomers of its cognate pattern recognition receptor (Fig. 2D). Those oligomers are themselves scaffolded by specific multivalent pathogen- or damage-associated structures. To mimic this effect, we employed a highly multimeric fusion partner, μNS (Schmitz et al., 2009). We first characterized the self-assembly of μNS-mEos3.1 by DAmFRET, revealing that it lacked a detectable saturating concentration (Fig. S2B). Therefore, yeast cells expressing μNS fusion proteins can be assumed to contain assemblies of those proteins even at low expression levels.

We therefore proceeded to fuse μNS to the ASC-, MAVS-, and HET-s-interacting signal transduction domains (Cai et al., 2014) of NLRP3, RIG-I, and NWD2, respectively. When expressed in trans, the NLRP3 PYD construct eliminated the low AmFRET phase of ASC; the RIG-I CARDs construct eliminated the low AmFRET phase of MAVS CARD; and the NWD2 ½ PrD construct eliminated the low AmFRET phase of HET-s PrD (Fig. 2E, diagonal plots). The μNS fusions therefore reduced the nucleation barriers to undetectable levels. This effect was entirely specific, as the fusions had no effect on the AmFRET distributions of non-cognate proteins (Fig. 2E, non diagonal plots). Taken together, these data confirm that ASC, MAVS, and HET-s activities are kinetically regulated by functional nucleation barriers.

The HET-s PrD has evolved rapidly and with low conservation of stabilizing structural elements (Daskalov et al., 2015b; Gendoo and Harrison, 2011). Nevertheless, very few point mutations disrupt the β solenoid fold that makes up HET-s prions (Daskalov et al., 2014; Wan and Stubbs, 2014). Paradoxically, two mutations that stabilize the fold appear to be unable to acquire it de novo in vivo (Daskalov et al., 2014). These observations suggest that the thermodynamic stability of the quinary structure is not as important for HET-s function as the size of the nucleation barrier that it imposes. We used DAmFRET to investigate.

We analyzed three hypomorphic mutants of HET-s PrD. One of these (N226A + N243A) disrupts both of the asparagine ladders that run along the spine of the β solenoid. The other two mutants (F286A and W287A) stabilize the β solenoid structure (Daskalov et al., 2014). We first asked if these thermodynamic effects manifest as changes to the level of AmFRET. To do so, we took advantage of the fact that HET-s (including the mutants characterized here) forms only a single functional quinary structure (Daskalov et al., 2014) that can be templated by NWD2 (Cai et al., 2014; Daskalov et al., 2015a). We therefore acquired AmFRET distributions in the presence of NWD2 ½ PrD-μNS. All cells, regardless of variant, exhibited intense AmFRET, confirming that nucleation barriers had been eliminated and all variants could indeed fold into the native quinary structure. The distributions of AmFRET values were Gaussian in all cases, indicating that steady state levels of structure had been achieved at the time of measurement. Therefore, any deviation from WT levels of AmFRET must result from a change in the equilibrium fraction of protein polymerized, and thereby the thermodynamic stability of the quinary structure. As expected, the destabilizing mutant reduced AmFRET whereas the stabilizing mutants increased it (Fig. 2F).

We next asked how, despite stabilizing the prion structure, F286A and W287A preclude prion formation de novo. To do so we used DAmFRET to evaluate nucleation barriers in the absence of a templating factor (Fig. S2C). We then divided each distribution into AmFRET-negative and AmFRET-positive cell populations, and plotted the cumulative distribution of the fraction of cells in the AmFRET-positive population (Fig. 2G). Each distribution was then fit to a stretched exponential function, the inverse slope of which correlates with each protein's nucleation barrier (see Methods and Table S1). For simplicity we report the inverse slope at the inflection point, a proxy for the conformational (concentration-independent) component of the nucleation barrier. Both mutants dramatically increased this value relative to WT. We conclude that the hypomorphic phenotypes of F286A and W287A can be attributed, at least in part, to a heightened nucleation barrier.

Supersaturability and spontaneous phase separation underlie prion behavior

Having established that nucleation-limited quinary assembly generates bimodal AmFRET distributions, we next asked if prion proteins broadly exhibit this behavior. We focused initially on the prion-forming domain (PrD) of the archetypal yeast prion protein, Sup35, which normally exists dispersed throughout the cytosol. However, approximately one in every ten million cells (Chernoff et al., 1999; Lancaster et al., 2010) acquires an amyloid structure that perpetuates itself indefinitely. Sup35 belongs to a large class of prion forming proteins characterized by low complexity sequences (LCS) enriched for polar, uncharged residues. Sequences of this nature are referred to as “prion-like”, even though they lack similarity to functional prion-forming proteins like ASC, MAVS, and HET-s (Halfmann, 2016).

When expressed in cells lacking pre-existing prions of endogenous Sup35, Sup35 PrD produced a strongly bimodal distribution of AmFRET values (Fig. 3B). Prion formation sufficed to localize cells to the high AmFRET population, because cells harboring pre-existing prions populated this state exclusively (Fig. 3A). We next asked if de novo acquisition of AmFRET coincides with bona fide prion nucleation. To do so we employed a genetic background that causes cells to accumulate red pigment when they contain soluble Sup35, but not when they contain aggregated Sup35 (Alberti et al., 2009). We used fluorescence-activated cell sorting (FACS) to isolate AmFRET-positive and AmFRET-negative cells expressing the same amount of Sup35 PrD, and then plated them to media that repressed its expression. Cells in the lower population formed red colonies, whereas cells in the upper population formed white and pink colonies (Fig. 3B and C), demonstrating that the AmFRET-positive cells had indeed acquired heritable (self-sustaining) structure that perpetuated to endogenous Sup35.

We next tested additional prion-forming LCS regions, including those from the yeast proteins Ure2, Rnq1, Swi1, Mot3, and Cyc8 (Alberti et al., 2009; Du et al., 2008; Patel et al., 2009; Sondheimer and Lindquist, 2000; Wickner, 1994). All exhibited bimodal distributions of AmFRET (Fig. 3D). This indicates that a) the proteins are supersaturable and b), their supersaturation is sporadically shattered by nucleated phase separation. The concentration-dependence and nucleation barriers differed dramatically between proteins (Fig. 3D and E), and in ways that generally recapitulated their known prion-forming tendencies. For example, cells expressing Rnq1 or the PrD of Mot3, each of which forms prions at relatively high frequencies spontaneously (Holmes et al., 2013; Liebman and Chernoff, 2012), also exhibited relatively low nucleation barriers. Cells expressing the Ure2 or Cyc8 PrDs, which form prions at much lower frequencies spontaneously (Liebman and Chernoff, 2012; Patel et al., 2009), exhibited relatively high nucleation barriers.

Finally, we asked if DAmFRET distinguishes “prion-like” proteins that form non-prion aggregates from those that actually form prions. For this purpose, we selected the highly “prion-like” regions of the yeast proteins Ngr1, Psp1, and Sla1. These had previously been determined using cytologic, biochemical, and genetic assays to form non-prion amyloid (Ngr1) or non-amyloid (Psp1, Sla1) aggregates in yeast (Alberti et al., 2009; Sun et al., 2015). When examined by DAmFRET, all three differed in a consistent way from prions: they acquired AmFRET as a continuous function of concentration (Fig. 3F and 3G), indicating negligible nucleation barriers and, hence, disorganized condensation. A closer look at Ngr1 LCS revealed that cells expressing it to high concentration actually partitioned into two populations ($p=1.43 \times 10^{-11}$, F-test) with slightly different AmFRET intensities (Fig. 3G), suggesting a nucleated transition consistent with amyloid formation. In summation, these data reveal two explanations for the absence of prion behavior among certain otherwise aggregation-prone LCS. Some of them lack the ability to form highly organized quinary structure over experimental timescales (Psp1 and Sla1 LCSs). At least one other (Ngr1 LCS) can form such a structure, but that structure appears to be only slightly less soluble than the disorganized quinary structure that preceded it. Hence, our data suggests that Ngr1 LCS forms prions, but may simply have failed to produce a phenotypic change large enough to be detected with the previous state-of-the-art (albeit low resolution) prion reporter, which links the color of yeast colonies to the solubility of a fusion protein (Alberti et al., 2009, 2010). That reporter also failed to detect prion behavior by Cyc8 and Mot3 PrDs (Alberti et al., 2009), both of which showed unambiguous nucleated transitions as revealed by DAmFRET (Fig. 3D).

The archetypal prion domain, Sup35 PrD, forms non-prion condensates

To test the resolution of DAmFRET in detecting differences in nucleation barrier, we took advantage of the fact that Sup35 nucleates only in the presence of pre-existing amyloids (known as [*PIN*+]) of another protein, Rnq1 (Derkatch et al., 2001). We therefore subjected Sup35 PrD to DAmFRET in cells containing different quinary structures of Rnq1 (Bradley et al., 2002). The nucleation barrier of Sup35 PrD to amyloid (Fig. 4A and B) increased in perfect agreement with the previously characterized ability of each Rnq1 structure to template Sup35 prions: high, medium, low, and absent (corresponding to fully dispersed Rnq1, or [*pin*-]).

Surprisingly, in the absence of Rnq1 amyloids, the nucleation barrier of Sup35 PrD to amyloid was insurmountable over the time scale of the experiment. Nevertheless, cells that contained deeply supersaturating levels of protein uniformly acquired a low level of AmFRET (Fig. 4B). A closer look revealed that the FRET radiated from small puncta in the cytosol. Some of these were larger than the resolution of our microscope (up to ~600 nm), allowing us to assess morphology (Fig. 4C). They were spherical (β, aspect ratio of 1.18 ± 0.02, n = 13). Amyloid puncta, in contrast, were highly aspherical (α).

Given their considerable stability against prion nucleation, we expected these spherical puncta to consist of amorphously aggregated, immobilized Sup35 PrD. We used half-FRAP measurements to probe their internal dynamics. The half-FRAP recovery curves fit to a two component exponential, corresponding to recovery times of 0.275 ± 0.110 s and 1.710 ± 0.197 s for fast and slow components, comprising 9 ± 2 % and 28 ± 4 % of the recovery, respectively. The fast component approached that of cytosolic diffusion recovery, 0.212 ± 0.008 s, as determined from cells expressing unfused mEos3.1. The slow component compared with that of whole punctum FRAP performed in the same cells, which revealed a recovery time of 0.864 ± 0.069 s. These data indicate that Sup35 PrD molecules diffuse rapidly inside the puncta -- almost as fast as free diffusion, but exchange relatively slowly with those in the bulk cytosol. Distinct fast diffusion inside the puncta is consistent with a phase separated system in which exchange across the phase boundary is slower than diffusion inside the condensate (Fig. 4D).

The internal dynamics and sphericity of these Sup35 PrD puncta resemble those of liquid droplets. To explore this possibility, we recorded their dynamics in living cells. The puncta were highly mobile. We observed two puncta within a cell coalescing into a larger punctum (Fig. 4E) whose fluorescence intensity exactly matched the sum of its precursor puncta (Fig. S4A). Note that the precursor puncta were significantly larger than the resolution of our microscope (diameters 410 nm and 500 nm). As a result, non-liquid contact between them would result in an elongated (aspherical) punctum. However, the coalesced punctum was instead spherical (aspect ratio 1.04, diameter = 490 nm). We conclude that Sup35 PrD undergoes liquid-liquid phase separation when overexpressed in the absence of amyloid templates.

This tendency of Sup35 PrD is consistent with its reported ability to substitute for a compositionally-similar region of TIA-1 in targeting that protein to mammalian stress granules (Gilks et al., 2004). The yeast ortholog of TIA-1, Pub1, also contains a PrD (Alberti et al., 2009; Li et al., 2014; Urakov et al., 2010) that forms liquid condensates (Lin et al., 2015). To test, if stress induces PrD condensation, we performed DAmFRET for Sup35 and Pub1 PrDs following exposure to the oxidative stressor, arsenite (10 mM for 1 hour). This treatment slightly decreased fluorescence of the donor and acceptor fluorophores (Fig. S4), which precluded a quantitative comparison of its effects on self-assembly. Nevertheless, arsenite increased AmFRET intensity in cells harboring non-prion states of Sup35 PrD ($p<0.005$, t-test of mean AmFRET, one-tailed, unequal variance) and Pub1 PrD ($p<0.05$), whereas it did not do so for cells harboring the corresponding prion states, or for cells expressing unfused mEos3.1 ($p>0.05$) or the non stress granule-associated protein, ASC PYD ($p>0.05$; see also Fig. S4). The fraction of Pub1 PrD-expressing cells, but not Asc PYD-expressing cells ($p>0.05$, t-test, one-tailed, paired), in the discontinuous high-AmFRET population also increased ($p<0.05$), suggesting that Pub1 PrD condensation reduces its nucleation barrier to amyloid.

We next investigated the effect of arsenite on Sup35 PrD using time-lapse microscopy. Consistent with its enhancement of AmFRET, arsenite strongly promoted droplet formation (Fig. 4F).

Sup35 PrD condensates are kinetically stable with respect to prion nucleation

To explore potential linkages between liquid and amyloid quinary states, we compared phase behaviors with and without amyloid templates for a range of Sup35 mutants that have been identified in the literature to either promote or inhibit prion formation.

In the presence of Rnq1 amyloids, all mutants behaved as expected (Fig. 5A). The prion-inhibitory mutants of Sup35, Y46K+Q47K and Q61K+Q62K (Bondarev et al., 2013), reduced the population of high AmFRET cells. The PrD^{N} mutant formed prions even more effectively than WT, as expected (Halfmann et al., 2011). Its reciprocal mutant, PrD^{Q}, completely eliminated the high AmFRET population, and instead produced a level of AmFRET intermediate to that of liquid droplets and prions. To determine if PrD^{Q} could nevertheless acquire an amyloid state, we repeated DAmFRET in cells containing pre-existing amyloids of endogenous Sup35. Amyloids of a particular structure ([*PSI*+(Sc4)], but not of [*PSI*+(Sc37)]; Tanaka et al., 2006) completely shifted PrD^{Q} to the high AmFRET state (Fig. S5), indicating that the non-amyloid assemblies of PrD^{Q} are in fact kinetically trapped en route to amyloid.

The propensities of the mutants for non-prion condensation became apparent when expressed in the absence of Rnq1 amyloids ([*pin*-]). Remarkably, the prion-inhibitory mutants Y46K, Q47K and Q61K, Q62K inhibited condensation (Fig. 5A). Sup35 PrD^{Q} again formed intermediate AmFRET species, consistent with its known tendency to form non-amyloid aggregates (Fig. 5B and Halfmann et al., 2011). PrD^{N} did not noticeably influence condensation, but unlike WT or any of the other mutants, it did enable the nucleation of a small population of prion-containing cells. These cells only arose at concentrations that supported liquid droplet-associated AmFRET, suggesting that the droplets may enable prion nucleation by permissive sequences even in the absence of heterologous templates.

We next analyzed a series of Sup35 PrD variants that contain an identical amino acid composition as the WT protein, but with the order of residues scrambled (Ross et al., 2005). One of these, #25, had been found to form prions much less efficiently than the others. DAmFRET indeed revealed a greatly reduced high AmFRET population for this variant (Fig. 5C). Intriguingly, however, the protein's ability to form liquid droplets was unperturbed, and these persisted in most cells even in the presence of Rnq1 amyloids. This indicates that the phase boundary for Sup35 PrD condensation to a liquid is not strongly impacted by amyloid templates. Therefore, Rnq1 amyloids appear to template Sup35 prion nucleation by specifically lowering the barrier for conformational nucleation rather than condensation.

Two of the other scrambles, #21 and #26, populated low- and high-AmFRET states almost indistinguishably from WT, revealing comparable propensities for condensate and prion formation. The one difference, however, is that unlike WT, they also nucleated prions at observable frequencies even in the absence of Rnq1 templates.

The final analyzed scramble, #24, produced DAmFRET unlike all of the other Sup35 constructs. Cells that lacked Rnq1 templates partitioned between separate low AmFRET and intermediate AmFRET populations. Both populations persisted in the presence of Rnq1 templates. However, a third population also emerged with a high AmFRET level indicative of the expected Rnq1-templated amyloid state. The appearance of this population coincided with a reduction in the fraction of cells harboring fully dispersed protein, while the fraction of cells harboring the intermediate AmFRET state remained unchanged. This result suggests that the intermediate state does not permit amyloid nucleation.

Using microscopy and FRAP to investigate further, we observed that the intermediate AmFRET state coincided with the acquisition of irregular foci with negligible internal dynamics (Fig. 5D). The amount of diffuse fluorescence outside of these foci was elevated with respect to that outside amyloid foci of the same protein. Taken together these observations indicate that #24 forms a novel ordered assembly that is less stable than amyloid, yet precludes its nucleation.

In total, the data from Sup35 variants support a two-step mechanism for de novo nucleation of amyloid in the cellular environment: the proteins first assemble into dynamic condensates that then lower the barrier to amyloid nucleation. Mutations that interfered with prion formation did so by altering the physical properties of that condensate: they either reduced its thermodynamic stability leading to fewer opportunities for conformational nucleation (Y46K+Q47K and Q61K+Q62K); increased its thermodynamic stability leading to greater conformational nucleation barriers (PrD^{Q} and #24); or reduced the protein's compatibility with endogenous templates again increasing the conformational nucleation barrier (#25).

Quinary structure can kinetically control proteotoxicity

We noticed that Sup35 PrD scramble #24 accumulated to lower concentrations than the other variants, specifically in cells that lacked Rnq1 amyloids ([*pin*-]) (Fig. 5C). We wondered if this might reflect a toxic consequence of the non-amyloid assemblies of this protein, as was previously reported for PrD^{Q} (Halfmann et al., 2011). To test, we plated serial dilutions of the cells to media that either induced or repressed ectopic protein expression. Variant #24, but none of the other scrambles, suppressed colony formation in cells lacking amyloids (Fig. 6A).

To determine if toxicity arises from a particular quinary state of the protein, we repeated the DAmFRET experiment in the absence of cell cycle arrest, and used the brightfield channel in imaging flow cytometry to evaluate the fraction of cells dividing (budding index) for each state of the protein. Variant #24 severely reduced this measurement of cell proliferation (Fig. 6B). Remarkably, the effect was entirely specific to its non-amyloid condensates: the high AmFRET population of cells that occurred in the presence of Rnq1 amyloids budded just as frequently as cells expressing unfused mEos3.1. Hence, the amyloids ameliorated toxicity by draining the cell of kinetically trapped quinary assemblies.

To evaluate the generality of this finding, we tested proteotoxic mutants of another low complexity yeast prion protein, Rnq1. Two mutants of Rnq1: L94A and L94A+L96A+L97A, had been previously discovered using cytological and biochemical analyses to differentially reroute the protein from amyloid to non-amyloid aggregates (Douglas et al., 2008). The non-amyloid aggregates sequester a spindle pole body component, resulting in aberrant cell cycle arrest. Amyloid aggregates of the same protein not only lack this effect; they rescue cells from it (Treusch and Lindquist, 2012). DAmFRET revealed that in addition to the high AmFRET, prion-associated state, the WT protein formed a concentration-dependent low intensity

AmFRET state resembling that of Sup35 condensates (Fig. 6C, top). This state is consistent with the protein's reported ability to form non-amyloid assemblies (Kroschwald et al., 2015). The mutant proteins also acquired both AmFRET levels, but with strikingly different distributions than that of WT. They lacked bimodality at all concentrations, and instead accumulated at intermediate AmFRET levels that steadily increased with concentration. Remarkably, AmFRET increased to levels of WT amyloid in cells harboring endogenous Rnq1 prions (Fig. 6C, bottom). Hence, the propensity of the mutants to form toxic, non-amyloid aggregates corresponds with kinetic arrest en route to an amyloid-like quinary structure. The strong relationship of AmFRET levels with concentration suggests that the aggregates become increasingly ordered as they grow. Future experiments will be required to test this interpretation. Nevertheless, we conclude that "prion-like" LCSs commonly form non-amyloid condensates, and aberrant stabilization of these condensates disrupts cell physiology.

DISCUSSION

Protein overexpression unmasks latent quinary structural tendencies

Nucleated quinary assembly constitutes a phase transition. The boundary that delineates whether or not a particular assembly can exist extends through all dimensions of phase space (Banani et al., 2017; Vekilov, 2012). Concentration is one dimension. Temperature, pH, and ligands are others. We reasoned that by pushing protein concentrations well above physiological levels, we can systematically reveal phase boundaries that are, nevertheless, potentially physiological in other dimensions of phase space (Fig. 7). We created a method, DAmFRET, to do so. We vindicated our approach with the discovery that Sup35 and Pub1 PrDs condense not only at high concentration during stress-free growth, but at lower concentrations under conditions that induce stress granules. Nevertheless, we acknowledge that over-expressing a protein does more than change its absolute concentration in the cell. It also changes its concentration *relative* to physiological factors like protein chaperones, and may induce cellular responses; both effects can influence quinary structure. Moving forward, DAmFRET offers a valuable tool to interrogate such effects genetically and pharmacologically.

Discoveries of new prion-forming proteins have tended to be phenomenological in nature (Alberti et al., 2009; Cai et al., 2014; Chakrabortee et al., 2016a, 2016b; Si et al., 2003; Yuan and Hochschild, 2017), with little quantitative understanding of how a given protein's ability to do so compares with that of other proteins. DAmFRET uniquely enables quantitative comparisons of quinary folding preferences for different proteins under the same experimental conditions. Prions by definition produce mutually exclusive cellular phenotypes, a characteristic that arises both from the magnitude of the underlying quinary assembly's nucleation barrier and the rapidity of achieving steady state, once nucleated. The degree of bimodality, as assayed by DAmFRET, therefore provides an operational measure of "prionness" at the cellular level. Prion proteins generated unambiguous bimodal distributions of AmFRET that quantitatively differed both between proteins and between experimental perturbations to nucleation barriers. Non-prion forming proteins did not produce bimodal distributions. Moving forward, DAmFRET will be adapted to evaluate "prionness" at the genetic level, as well. By simply acquiring a second DAmFRET measurement following a transient period of query protein repression and cell cycling, the mitotic heritability of nucleated states for any protein can, in principle, be quantified.

Quinary structure exerts kinetic control

Quasi-two-dimensional polymerization has evolved independently in multiple branches of innate immunity (Cai et al., 2014; Daskalov et al., 2015b; Kajava et al., 2014; Li et al., 2012; Lu et al., 2014). In addition to death folds and HET-s, we can now include sesA, a putative prion determinant and signaling protein of *Nectria haematococca* (Daskalov et al., 2012). The proliferation of death folds in metazoans (the human proteome contains 70 death fold proteins in addition to MAVS and ASC), and the extensive diversification of HET-s-like amyloid motifs in fungi and humans (Daskalov et al., 2015b; Kajava et al., 2014), indicates an important signaling activity made possible by this type of quinary structure, and not by one dimensional polymers, which evolve relatively easily (Garcia-Seisdedos et al., 2017). In fact, polymerization is not even required for the proteins' biochemical activities: dimerization suffices to activate MAVS (Tang and Wang, 2009), and only the terminal monomer of a HET-s prion particle engages downstream effector proteins (Seuring et al., 2012).

Our data lead us to propose that the essential function of quasi-two-dimensional polymerization is kinetic control via nucleation -- a fundamentally multidimensional phenomenon. Innate immune signaling pathways have evolved to decide cell fate based on inputs as infinitesimal as an individual molecule of viral dsRNA -- far too small to drive a cell-wide change in protein activity thermodynamically. Kinetic control enables the proteins themselves to drive that change. Analogous to damming a river, the nucleation barrier allows the proteins to accumulate to supersaturating concentrations, and in doing so, store the energy of thousands of potential intermolecular bonds. A single nucleating event collapses the barrier, releasing the energy in explosive fashion. Pathogen-sensing proteins trigger that event by binding the viral dsRNA (or other foreign multivalent scaffolds) resulting in their oligomerization into a quinary structural nucleus that then propagates that structure throughout the pool of molecules.

Condensation enables environmentally responsive compartmentalization

All of the innate immune signaling proteins we characterized underwent nucleated polymerization directly from dispersed monomers, with no evidence of metastable condensed phases. The other group of proteins we characterized here, "prion-like" proteins, tended to behave differently. Many produced condensates.

"Prion-like" describes sequences that resemble the canonical yeast prion proteins: Ure2, Sup35, and Rnq1 (Alberti et al., 2009; Cascarina and Ross, 2014). They tend to be lengthy and replete with polar uncharged residues, particularly glutamine and/or asparagine. These features do not directly promote amyloid (Goldschmidt et al., 2010; Knowles et al., 2014; Maurer-Stroh et al., 2010). Instead, they promote liquid-like condensation by increasing low affinity polyvalency

(Banani et al., 2017; Halfmann, 2016). As elaborated below, condensates can, in turn, engender amyloid nucleation.

Unlike polymers, condensates contain little internal structure. Their nucleation therefore coincides with probabilistic fluctuations in density (but not conformation), resulting in a relatively small nucleation barrier, consistent with our observations (Fig. 1E, and 4D). Nature exploits this to compartmentalize subcellular processes such as transcriptional and post-transcriptional gene regulation. The constituent protein monomers do not accumulate to highly supersaturating levels. Instead, they dynamically condense and evaporate in tune with changes in thermodynamic parameters like temperature, pH, and ligand concentrations (Banani et al., 2017; Falahati and Wieschaus, 2017; Riback et al., 2017).

We discovered that the archetypal yeast prion domain, of Sup35, forms non-prion liquid condensates. This capability of the protein is masked in most laboratory strains by the presence of heterotypic amyloid templates of Rnq1. However, most yeast in the wild do not contain these templates (Halfmann et al., 2012; Nakayashiki et al., 2005), suggesting that disordered condensates of Sup35 are more likely than prions to govern its activity physiologically.

Condensation commonly functions to sequester energy-burning enzymes under times of stress (Petrovska et al., 2014; Riback et al., 2017; Saad et al., 2017; Wallace et al., 2015). The rapid formation and internal dynamics of Sup35 PrD droplets suggest that they too, may be optimized for storage and subsequent dissolution. That Sup35 self-assembly could serve a stress-protective role at the cellular level has been speculated due to its functional and compositional similarity to other stress granule proteins (Chernoff, 2007). Our results lead us to believe that Sup35 PrD, and “prion-like” sequences more broadly, function to compartmentalize intracellular biochemistry in a dynamic and thermodynamically-responsive fashion. The physiological parameters that control their assembly will differ for each protein, and in most cases await discovery.

Based on the fluorescence intensity and size of the droplets, we estimate that Sup35 PrD existed at millimolar concentrations within them. This corresponds to at least ten thousand-fold supersaturation with respect to the concentration of monomer that remains dispersed in amyloid-containing cells (approximately 50 nM; Tanaka et al., 2006). And yet, even though it remained fully mobile within the droplets, the protein failed to form amyloid on cellular timescales. That the WT sequence may have evolved to this level of supersaturability is supported by the fact that randomly scrambling it reduced fluidity -- either directly (#24) or by permitting prion nucleation (#25 and #26). The nucleation barrier therefore appears to functionally preserve activity by limiting liquid-to-solid transitions. The extraordinarily low saturating concentrations of amyloids (Knowles et al., 2014) tend to deplete protein from liquid condensates and other cellular binding partners, to levels that can be insufficient for survival (McGlinchey et al., 2011).

An evolving paradigm for prion-like sequences

Protein condensates are inherently metastable with respect to ordered assembly (Halfmann, 2016; Vekilov, 2012), and physical features of the polypeptide backbone guide that assembly toward amyloid (Knowles et al., 2014). Protein condensates therefore tend to become less dynamic with time as the polypeptides settle into increasingly stable, amyloid-like configurations.

This transition can happen suddenly, via amyloid nucleation within the condensate, a phenomenon that has been well supported by theory and in vitro experimentation (Auer et al., 2012; Serio et al., 2000; Vekilov, 2012; ten Wolde and Frenkel, 1997). We uncovered evidence that Sup35 and Pub1 amyloids can nucleate through this two-step mechanism in the cellular milieu. We suspect the enhancement of condensation by stress, as reported here and elsewhere, followed by subsequent amyloid nucleation, may underlie stress-induced prion nucleation (Doronina et al., 2015; Holmes et al., 2013; Suzuki et al., 2012). The potential adaptive and maladaptive consequences of this quasi-Lamarckian phenomenon remain to be fully elucidated.

The solidification of condensates can also happen gradually (Banani et al., 2017; Halfmann, 2016). Our experiments revealing a graded stabilization of mutant Rnq1 assemblies indicate that at least one prion-like LCS can become kinetically frustrated throughout its quinary folding landscape. We speculate that as newly synthesized mutant Rnq1 polypeptides engage with pre-formed condensates, they fold into a slightly more ordered configuration than the polypeptides that preceded them. They then, in turn, template the next layer of incoming polypeptides to an even more ordered configuration. Such a progression in quinary structure would, in effect, record the thermodynamic history of the condensate. The breadth of this phenomenon among “prion-like” LCS and the extent to which nature has utilized it have not yet been explored. Excitingly however, at least two prion-like LCS form quinary structures implicated in biological memory: CPEB in certain invertebrates, and Whi3 in yeast (Caudron and Barral, 2013; Si and Kandel, 2016).

Condensate metastability underlies proteopathic aggregation

Does a vulnerability to quinary “misfolding” lie at the core of age-associated human degenerative diseases linked to “prion-like” proteins? Our data suggests it might. We found that proteopathic “prion-like” proteins, whether natural or experimentally derived, fail to remain dynamic or dispersed when supersaturated. Two mutants of Sup35’s PrD shifted the material properties of its condensates from liquid-like to solid, and these also rendered it proteotoxic. Proteotoxic mutants of Rnq1 likewise promoted its acquisition of non-amyloid solids. Finally, the ALS-associated prion-like protein, hnRNPA1, produced an AmFRET distribution that resembled these proteotoxic prion mutants, rather than their prion-forming WT counterparts.

We demonstrated that toxicity could be ameliorated by bypassing the vulnerable condensed phase. Providing amyloid templates to proteotoxic yeast prion mutants provided a shortcut to an even deeper energy well that depleted protein from toxic condensates and restored cell health. These observations support the paradigm that disease-associated proteotoxicity results more from stable non-amyloid assemblies than amyloids (Halfmann, 2016; Knowles et al., 2014).

Concluding remarks

Unlike protein folding at the secondary, tertiary, and quaternary levels, quinary "folding" can be rate-limited over biological timescales by nucleation. The larger the nucleation barrier, the more discrete the protein's distribution (Zhao and Moore, 2003), and hence the more precise its regulation by cellular and environmental factors that lower the barrier. Quinary folding therefore offers a level of regulatory precision that is simply not possible with lower levels of structure. At the extreme, it allows a single molecular event to completely alter the cellular activity of a protein. Nature has acted upon protein kinetics at the ensemble level.

Some features of quinary structure have therefore evolved according to their effects on nucleation barriers, rather than enzymatic activities and ligand interfaces that tend to shape protein evolution at lower structural levels. This indicates relationships between quinary structure and function that otherwise seem superfluous. Disordered protein condensates tend to have small nucleation barriers that limit their functions to subcellular spatiotemporal scales. In contrast, ordered assemblies such as amyloids have large nucleation barriers enabling them to function over organismal spatiotemporal scales. To some extent, then, the material existence of a particular quinary structure is irrelevant to its function. Testing this idea, its generality among protein condensates, and its potential contribution to their time-dependent cellular activities, presents a fantastic challenge for the future. The methods developed here provide ways to overcome this challenge.

Author Contributions

Conceptualization, T.K., T.S.K., E.K., and R.H.; Methodology, T.K., T.S.K., E.K., R.H., and ; Investigation, T.K., T.S.K., J.W., E.K., S.V., J.J.L., A.R.G.; Formal Analysis, T.K., T.S.K., J.W., E.K., S.V., J.J.L., A.B., J.R.U., and R.H.; Data Curation, M.C.; Visualization, T.S.K., and R.H., Writing – Original Draft, R.H.; Writing – Review & Editing, M.C., S.V., T.S.K., J.J.L., J.R.U. and R.H.; and Funding Acquisition, R.H.

Acknowledgements

We thank Susan Liebman and Jonathan Weissman for variant [*PIN*+] and [*PSI*+] yeast strains, respectively; Eric Ross for scrambled Sup35 PrD cloning templates; Boris Rubinstein, Simon Alberti, and Rohit Pappu for insightful discussions. We thank Mark Miller and Chris Wood for assistance preparing illustrations, and Michelle Tan for assistance with molecular biology. This work was funded by NIH Director's Early Independence Award DP5-OD009152, NIH grant P30 AG035982, and the Stowers Institute for Medical Research.

Methods

Cloning procedures

A gateway destination vector, BB5b, was constructed by ligating a GeneArt String encoding a yeast codon-optimized 4x(EAAAR) linker and mEos3.1 between HindIII and XhoI in pAG426GAL-ccdB (14155). The *URA3* promoter was truncated to increase plasmid copy number (Loison et al., 1989). A golden gate (Engler and Marillonnet, 2013) cloning-compatible vector, V08 was constructed from BB5b using gap repair to replace the Gateway cassette with inverted BsaI sites. V08 was then used to construct V12 by ligating a synthetic fragment encoding yeast codon-optimized mEos3.1-4x(EAAAR) followed by inverted BsaI sites between SpeI and XhoI. Finally, vector CA was constructed from V12 using gap repair to replace the inverted BsaI sites with the Gateway cassette.

Inserts available as pre-existing Gateway entry clones (Alberti et al., 2009; Cai et al., 2014; Douglas et al., 2008; Halfmann et al., 2011) were introduced into BB5b and CA using Gateway LR recombination. The Rnq1 constructs used for Fig. 6 (but not Fig. 3) contain a non-native cysteine at the N-terminus, which is encoded in the Gateway entry clones (Douglas et al., 2008) used for their construction.

All other inserts were ordered as GeneArt Strings flanked by Type IIs restriction sites for ligation between self-excising BsaI sites in V08 and V12. All plasmids were verified by sequencing. Table S2 lists the plasmids and encoded polypeptide sequences for all fusion proteins characterized in this study.

Yeast genetic manipulations

Table S3 details all yeast strains used in this study. Yeast were transformed with a standard lithium-acetate protocol (Gietz et al., 1992). The primary DAmFRET strain, y1713, was constructed from Y7092 (Tong and Boone, 2007). PCR-based mutagenesis (Goldstein and McCusker, 1999) was used to replace *CLN3* in its entirety with a purpose-built cassette that expresses *WHI5* from the inducible *GAL1* promoter. Strains y1851 and y1852 were constructed by passaging strains Y7092 and y1713, respectively, four times on YPD plates containing 3 mM GdHCl, a prion-curing agent (Ferreira et al., 2001). Strain y1734 is a mating type-converted derivative of y1713. It was used to make y1903 by omega replacement (Hastings et al., 1993) of the ho locus with a purpose-built cassette that expresses a tandem pair of *URA3* ORFs (from *Candida albicans* and *Kluyveromyces lactis*) from a doxycycline-repressible promoter (tetO7) followed by 4x(EAAAR)-µNS-4x(GGGGS)-mTagBFP2 (cassette sequence available upon request). Strains y1945, y1985, and y1986 were constructed by chromosomal replacement of the tandem *URA3* ORFs with synthetic ORFs encoding NWD2 ½ PrD (residues 1-50), RIG-I CARDs (residues 1-200), and NLRP3 PYD (residues 1-95), respectively, thereby enabling the expression of those proteins as fusions to 4x(EAAAR)-µNS-4x(GGGGS)-mTagBFP2 when doxycycline is omitted from the media.

*GAL1*pr-mediated overexpression of *WHI5* in a *cln3*-knockout background potently arrests cells in G1 (Adames et al., 2015), thereby preventing nucleated protein assemblies from transmitting beyond the original cell, while enabling more accurate calculation of cell volume due to the spherical shape of the arrested cells. Growing the yeast in glucose-based medium enables the cells to proliferate, whereas switching them to galactose-medium induces arrest and simultaneous induction of fusion protein expression.

Preparing cells for DAmFRET

Standard yeast media and growth conditions were used. Single transformant colonies were inoculated to 200 µl of glucose-containing selection medium per well in a round bottom microplate, then incubated on a Heidolph Titramax vibrating platform shaker at 30℃, 1350 RPM overnight, to allow for the prevalence of a range of copy numbers of plasmid in the population and to obtain a turbid culture. Cells were then washed twice with sterile distilled water to remove residual glucose before being resuspended in 200 µl of galactose-containing induction medium and returned to the incubating shaker for approximately 16 hrs. Microplates were then illuminated with an OmniCure® S1000 fitted with a 320-500 nm (violet) filter and a beam collimator (Exfo), positioned 45 cm above the plate, for a duration of 25 min, which was found to produce the maximum acceptor fluorescence with minimal photobleaching of donor. Violet light induces cleavage in the mEos3.1 peptide backbone adjacent to the chromophore (Wiedenmann et al., 2004; Zhang et al., 2012), converting it from a green form (emission peak at 516 nm) to a red form (emission peak at 581 nm). The beam power at the plate was 11.25 mW/cm^2, giving a total photon dose of ~17000 mJ/cm^2. Microplates were shaken at 800 RPM on a microplate shaker during photoconversion to prevent cell settling.

DAmFRET Data Collection

All the AmFRET data were acquired on an ImageStream$^{®x}$ MkII imaging cytometer (Amnis) at 60X magnification with low flow rate and high sensitivity using INSPIRE software. INSPIRE software directed the instrument to acquire as follows: channel 04 (brightfield in camera one), channel 10 (brightfield in camera two), channel 02 (donor fluorescence), channel 03 (sensitized emission FRET), channel 07 (blue fluorescence, a proxy for dead/dying cells as validated by staining with Sytox Far Red; see Supplemental Fig. 1A) and channel 09 (acceptor fluorescence). Magnification at 60X provided a pixel size of 0.3 µm^2. All samples were loaded from the microtiter plate using the ImageStream$^{®x}$ MkII autosampler. Channels 02 and 03 captured emission from 488 nm excitation, with 577/35 nm and 528/65 nm filters, respectively. Channel 07 captured emission from 405 nm excitation, with a 457/45 nm filter. Channel 09 captured emission from 561 nm excitation, using a 582/25 nm filter.

Brightfield-based gates were assigned in INSPIRE: first for focused events, determined by gradient root mean squared, and second for single cells, determined by area and aspect ratio. These focused, single-cell events were counted for donor and acceptor fluorescence positivity. For each sample, a minimum of 20,000 double positive events or maximum of between 5 and 10 minutes collection time were counted before proceeding to the next sample. Although only putative target events were counted, all unsaturated events were acquired and saved.

Compensation of the data collected was performed by using the built in wizard of IDEAS 6.2 on single color controls – cells expressing non-photoconverted mEos3.1 and those with dsRed2 (as a proxy for the red form of mEos3.1).

DAmFRET Data Analysis

Data were processed using IDEAS 6.2 (Amnis) software and batched using FCS Express Plus 6.04.0015 software (De Novo). IDEAS yields standard parameters, such as integrated intensity of acquired channels, as well as user-derived features, such as AmFRET (FRET intensity/acceptor intensity). To measure cell area from brightfield, we created a feature for area calculated by the adaptive erode mask, with an adaptive erosion coefficient set at a threshold of 70%, which both visually aligns with the cell boundary and corresponded to mean cell area from a culture simultaneously measured by microscopy. All integrated intensity values reported or intensity derived features (e.g. cytosolic concentration) exclusively represent intensity within this brightfield mask.

AmFRET positive population fractions were determined by dividing cytometry histograms into 64 bins logarithmically spaced from 1 to 1000 micromolar. For each protein, the threshold for the AmFRET positive population was measured as the point halfway between the two population centers as determined by a multi-Gaussian fit of the AmFRET distribution. For strains where only the positive or negative population are observed, the threshold value was determined by a closely related protein showing both populations. For each bin, the fraction of cells in the AmFRET positive population was determined. Bins at the low and high extremes of concentration were excluded when their fractions deviated above and below, respectively, neighboring bins due to low event number and autofluorescence. These curves were then fit to an inverse stretched exponential function using non-linear least squares optimization via the Levenberg-Marquardt method (Bevington and Robinson, 2003):

$$F_{pos} = 1 - exp\left[- ln(2) \cdot \left(\frac{c - c_{min}}{EC50 - c_{min}}\right)^{\alpha}\right],$$

where c is the concentration, *EC50* is the concentration at which the AmFRET positive population is equal to 50%, c_{min} is the minimum concentration for nucleation (below which F_{pos} must be 0). The parameter, α, is a somewhat abstract parameter relating the rate of rise in FRET positive population with concentration. As a result, we instead report the slope at the EC50 value: $S = \frac{ln(2) \cdot \alpha}{2 \cdot EC50}$. This equation was chosen because it describes the data well, and unlike the oft-used sigmoidal functions, goes to 0 at concentrations below the minimum concentration. While this may not be crucial for the current study, we anticipate that it will be important for theoretical considerations in future work. Errors were obtained by the monte carlo method, employing random noise added to the best fit curve with a standard deviation equal to the fit residuals standard deviation. 100 such randomized curves were fit to obtain standard errors in the fit parameters.

For the Ngr1 LCS, the distribution of AmFRET values for cells containing at least 100 µM was fit to a double Gaussian function as with the stretched exponential fitting above. An F-test (Bevington and Robinson, 2003) was performed to determine the significance of a double vs. single Gaussian fit.

Determining absolute protein concentration from fluorescence intensity

Molecular brightness of photoconverted mEos 3.1 was calibrated by ImageStream$^{®x}$ MkII measurement of mEos3.1 endogenously fused to Spc42, a protein in S. cerevisiae with about 1000 assembled molecules per cell (Bullitt et al., 1997), in order to relate instrumental intensity values to molecule number. Our calibration method is based on methods from fluorescence correlation spectroscopy (Müller, 2004; Shivaraju et al., 2012; Slaughter et al., 2011). Brightfield area measurements generated by the instrument permitted extrapolation from cell size and Spc42-derived molecular brightness to gross cellular concentration. Given that organelles occupy about 17% of haploid S. cerevisiae cell volume (Uchida et al., 2011), we corrected the calculation to reflect concentration from fluorescence intensity generated in the cytosol.

The method firstly consists of the measurement of unconverted mEos3.1 molecular brightness as defined by the peak intensity observed by a single mEos3.1 molecule using Spc42 as a reference standard. One attractive feature of the spindle pole body is that its size of ~150 nm (Bullitt et al., 1997) is significantly smaller than the resolution of the imaging cytometer. As a result, the observable spot on the imaging cytometer is the same size as would be expected from a single fluorescent molecule and its peak amplitude will be proportional to a single molecule brightness multiplied by the fluorophore copy number.

Cells expressing Spc42-mEos3.1 were acquired on the ImageStream at 40, 80, 160, and 400 mW 488 nm laser powers. The IDEAS software was utilized to filter for unbudded and live cells based on scatter plots of area vs. aspect ratio and fluorescence intensities in ch02 vs. ch07, respectively. Compensated images were exported as 16-bit tiff images for visualization and further analysis with a custom implementation of the Bio-Formats plugin for ImageJ. Spc42 spots were clearly resolved in approximately 10% of the cells. The cells without clearly resolvable spots could have been out of focus. The maximum intensity in each image was selected as the initial center point of the Gaussian function. Gaussian fitting for the maximum spot in each image was then accomplished with a custom grid search fitting algorithm in ImageJ available at http://research.stowers.org/imagejplugins. The plugin attempts to fit a Gaussian function centered at each 0.25 pixel increment within 2 pixels in either direction from the maximum and with standard deviations from 0.5 pixels to 4 pixels at 0.1 pixel increments. At each candidate grid point, the fit is performed with linear least squares to a Gaussian function as follows:
$I(x,y) = b + Ae^{(x-xc)^2/2\sigma}e^{(y-yc)^2/2\sigma}$,
where *xc* and *yc* are the candidate centers of the actual spot, σ is the candidate spatial standard deviation. Linear least squares solves for the background intensity, *b*, and the peak amplitude, *A* at each candidate grid point. The point with the lowest χ^2 value is chosen as the best fit.

After fitting, a 2D histogram of peak amplitude vs. standard deviation reveals two behaviors. At small standard deviations there is a downward trending shoulder showing decreasing amplitude with increasing standard deviation. This is expected behavior for particles at different focal planes of the microscope. At higher standard deviations, the amplitude does not depend on standard deviation and these spot sizes correspond to values much larger than the expected resolution of the image cytometer (> 1 µm). This seems to correspond to the ~90% of cells that did not show visible spots as mentioned above.

A histogram was made of peak amplitudes with standard deviations less than 1.1 pixels (widths less than 850 nm). We estimate the standard deviation of the smallest spots to be 0.9 pixels (width of 700 nm), so this allows for a narrow distribution of spot sizes around the minimum value. These histograms as a function of laser power are shown in Fig. S1E. This histogram was then fit to a one dimensional gaussian function, this time using traditional non-linear least squares to obtain the center of the peak amplitude distribution. At 40 mW, the Spc42 peaks become more difficult to resolve and the peak amplitude distribution appears bimodal. The higher amplitude peak follows the trend from the other laser powers and represents “real” Spc42 spots.

The relationship between Spc42 peak amplitude and laser power is not linear (Fig. S1E). In order to create a calibration curve for different laser powers, the center of the peak amplitude distribution as a function of laser power was fit to a simple exponential function as follows:

$A = A_{max} \cdot (1 - e^{-P/x})$,

where P is the laser power, A is the peak amplitude, and A_{max} and x are fit variables. For our setup, A_{max} and x are 70.16 and 226.1, respectively. The brightness per mEos3.1 molecule is then obtained by simply dividing the A_{max} value by 1000 molecules. Our brightness per molecule for unconverted mEos3.1 is therefore 0.00594.

Now that we can derive the molecular brightness of green unconverted mEos3.1 at each laser power, we can use the integrated intensity from each cell to calculate the fluorophore concentration. Firstly, we use the measured area of each cell (from the Ideas software) in pixels to calculate the average intensity per pixel. From fluorescence correlation spectroscopy theory, we know that the average intensity is the product of the number of molecules in the focal volume multiplied by the molecular brightness of each molecule. In turn, the number of molecules per focal volume can be converted to concentration as follows:

$C = N/(N_a V_{focus})$,

Where N_a is Avogadro's number and V_{focus} is the microscope focal volume. The latter can be somewhat difficult to determine because of the poorly defined z dimension of the imaging cytometer focus. If we measure the average peak intensity of sub-resolution beads at differing shifts of the objective from the center of the flow stream, we obtain an approximate focal volume profile (Fig. S1D) with a width of 4.2 µm. Therefore we have chosen to treat the focal volume as a cylinder with radial gaussian profile of width 700 nm and a z extent of 4.2 µm, giving a focal volume of 2.7 μm^3 or 2.7 fL.

The final piece is to calibrate the photoconversion efficiency. We have chosen to express our concentrations in unconverted mEos3.1 concentration units as measured in the green channel. As a result, we can measure the average ratio of the intensity of a photoconverted cell in the red channel to an unconverted cell in the green channel. That ratio allows us to convert photoconverted red intensity into unphotoconverted green intensity for every sample and subsequent concentration calibration. In addition, we assume that most of the proteins analyzed will be cytoplasmic. The ratio of cytoplasmic to total volume in a yeast cell has been estimated as 0.83 (Uchida et al., 2011).

To summarize, cytosolic concentration ($C_{cytosol}$) assessment contains three derivations.

1) Determine the relationship between laser power and photoconverted donor intensity of a 1000 molecule complex
2) Find the conversion factor from integrated intensity to concentration given optic constraints (especially focal volume) of the instrument's 60x objective
3) Relate the photoconversion ratio of photoconverted green intensity to photoconverted red intensity of the mEos-only control

This last piece is crucial given that AmFRET signal accompanying mEos association is necessarily accompanied by loss of donor signal, whereas acceptor is constant and thus is an appropriate, AmFRET signal independent measure of fluorescent mEos. We can simplify the derivation above to represent the average concentration in the cytoplasm of a cell as:

$$C_{cytosol} = I_{red} k / A \, ,$$

where I_{red} is the compensated cell intensity in the red channel and A is the cell area in μm^2. Here, the multiplier, k, is as follows for 20 mW laser power:

$$k = \frac{mEos\ molecular\ brightness \cdot pixel\ area\ (um^2)}{focal\ volume \cdot ratio\ of\ cyto\ to\ cell\ volume} \cdot \frac{photoconverted\ donor\ mEos}{photoconverted\ acceptor\ mEos} = 0.0157 \cdot 2.45 = 0.038$$

Spot counting

Spot counting was performed using IDEAS software by creating a spot mask, peak mask, and range mask on Ch09 images and applying the spot count feature to the resulting mask.

Confocal imaging, time-lapse, and FRAP Analysis

Confocal images were acquired on an Ultraview Vox Spinning Disc (Perkin Elmer). The green form of mEos3.1 was excited using a 488 nm laser through either an alpha Plan Apochromat 100x 1.46NA objective (Zeiss) or a Plan Apochromat 63x 1.4NA objective (Zeiss). Emission was collected with an EMCCD (Hamamatsu, C1900-23B) and was filtered with a 525-50 nm bandpass filter. Movies were acquired with cells trapped in a CellASIC Onix2 microfluidic device (Millipore) with either single confocal slices or z-stacks. The z step spacing for movies was set to between 0.3 and 1 μm. The time scale between images varied. FRAP was acquired on the same system in FRAP preview mode, with 5 pre-bleach images and an appropriate time-lapse and length for recovery (every 60 ms for 10 s for half and full FRAP of liquid droplets). Images were expanded with bilinear interpolation for optimal visualization.

For half FRAP analysis, each recovery curve was collected, then normalized to minimum and maximum. Then a group of at least 19 curves were averaged together and fit with a two component exponential recovery function. 5 replicates of this process yielded 5 sets of fit components that were then averaged together (n = 141 total) to yield the final results. For full FRAP, each curve was fit with a one component exponential recovery function. All fits were averaged together to yield the final results (n = 28). Monomer control FRAP was treated the same way as full FRAP (n = 70).

Sphericity analyses were limited to thresholded puncta with sizes > 350 nm.

Sup35 colony color assay

Photoconverted yeast cells were sorted 750 events each from high and low AmFRET populations by a BD Influx Sorter each into 200μl of SD CSM. Subsequently, the media containing sorted cells were spread with glass beads onto ¼ YPD plates; these plates enhance visualization of color effects subsequent to adenine deficiency for the Sup35-C red/white colony assay (Alberti et al., 2009). After growth at 30°C for 2–3 days, plates were moved to 4°C overnight to deepen the red coloration, and photographed the following day.

Table S1. Parameters of fits of DAmFRET datasets

Table S2. Plasmids used and polypeptide sequences characterized in this study

Table S3. Yeast strains used in this study

Figures

Figure 1. Distributed Amphifluoric FRET distinguishes quinary assembly mechanisms
(A) Violet light photoconverts mEos3.1 from a green to a red form. The emission (solid curves) and excitation (dotted curves) spectra for the green and red forms are shown; and the region of overlap between them, responsible for FRET, is shaded in yellow.
(B) Schematic summarising the genetic strategy of using a strong inducible promoter (*GAL1*) to drive the expression of the query protein-mEos3.1 fusion, encoded by a plasmid with high copy number variation; resulting in a wide range of protein expression in the culture of yeast cells.
(C) Cartoon depicting DAmFRET. A culture of cells as in (B) is shifted to medium that simultaneously induces query protein expression while arresting cell division, resulting in large, spherical cells that accumulate the query protein to a wide range of concentrations.
Non-colinearity of the 488 nm and 561 nm lasers in the ImageStream$^{®x}$ MkII ensures that direct and sensitized emission (FRET) of the acceptor can be distinguished. See also Fig. S1.
(D) Schema depicting different forms of quinary structure. Arrows indicate the direction of order acquisition.
(E) DAmFRET plots of proteins representing each of the quinary forms in (D). A dashed line approximates mean AmFRET values of cells expressing fully monomeric protein. At least 20,000 cells are represented on each plot.

Supplemental Figure 1. Related to Fig. 1C
(A) Autofluorescence accurately distinguishes live from dead cells. Yeast cells expressing mEos3.1 (not photoconverted) were stained with Sytox Far Red. A histogram of Sytox intensity for single cells is shown on the left, and the Sytox-positive population ("dead") is colored red in the dot plot of blue autofluorescence (405 nm excitation, 457/45 nm emission) vs. mEos3.1 expression on the right. Based on this relationship, DAmFRET experiments excluded the population with blue autofluorescence and lacking detectable mEos3.1 fluorescence.
(B) The indicated proteins were expressed in isogenic [*psi*-] [*rnq*-] or [*PSI*+] [*RNQ*+] strains and tested for donor intensity prior to photoconversion and then for acceptor intensity following photoconversion. Samples containing amyloid are indicated in red; non-amyloid structured assemblies in blue; and unstructured or monomer in black. The linear regression (R^2 = 0.9728) indicates that mEos3.1 photoconversion is independent of fusion, expression level, or structure.
(C) Density plot showing tight correlation of donor and acceptor fluorescence of mEos3.1 following the photoconversion step.
(D) Left-right: A sample image of Spc42-mEos3.1 from the ImageStream$^{®x}$ MkII, a 2D density histogram showing the relationship between Spc42 spot size and peak amplitude showing the selected population for analysis, and a plot of the peak amplitude of beads on the ImageStream

as a function of objective focus Z Shift showing the shape of the focal volume (See Methods).
(E) Left: histograms of Spc42-mEos3.1 peak amplitude at different laser powers and Right: the trend of the centers of these histogram peaks (See Methods).

Figure 2. Quinary structure kinetically controls protein function
(A) DAmFRET plot of human ASC. See also Fig. S2A.
(B) Montage of cells inducing ASC protein expression, depicting switch-like acquisition of puncta. Images represent sum projection of confocal slices captured at 63X magnification.
(C) DAmFRET plots of CARD domain of MAVS, prion-forming domain (PrD) of HET-s, and SesA revealing bimodal distributions of AmFRET. A loss-of-function mutation in MAVS CARD (E26A) prevents assembly.
(D) Schema of the biological activation (top) of MAVS, HET-s and ASC; and experimental approach (bottom) to do so in the absence of cognate pathogen activators. The signal transducing domains of RIG-I, NWD2, and NLRP3 were fused to the constitutively self-assembling protein μNS. See also Fig. S2B.
(E) DAmFRET plots of MAVS CARD, HET-s PrD and ASC (ordered by columns) in cells that simultaneously express the indicated non-fluorescent μNS fusions (ordered by rows).
(F) Mean AmFRET values of HET-s variants templated by μNS-NWD2 ½ PrD. Error bars represent 95% CI from duplicate experiments. ****, p<0.0001 (ANOVA).
(G) Stretched exponential fits (see Methods) of the cumulative distribution of the fraction of high-AmFRET cells expressing different HET-s variants. The values (± SD) of the inverse slope at the inflection point, a proxy for the conformational (concentration-independent) component of the nucleation barrier, are indicated.

Supplemental Figure 2. Related to Fig. 2
(A) Representative image panel showing a typical cell identified by the Spot Count feature from the AmFRET data of Asc. The panels are (left to right) donor, FRET, acceptor, and bright field merged with acceptor signal
(B) DAmFRET plot of μNS-mEos3.1 showing self-assembly at all concentrations.
(C) DAmFRET plots of HET-s mutants in the absence of a templating factor.

Figure 3. Supersaturability and spontaneous phase separation underlie prion behavior
(A-B) DAmFRET plots of Sup35 PrD in cells with amyloids of endogenous Rnq1 ([*PIN*+]) and with (A; [*PSI*+]) or without (B; [*psi*-]) amyloids of endogenous Sup35.
(C) Representative images of colonies of cells (with the red-white colony reporter) derived from AmFRET-positive (α) and -negative (ß) gates similar to that marked in (B).
(D) DAmFRET plots of known yeast prion forming sequences.
(E) Stretched exponential fits of the data from (D), as in Fig. 2G. The values of the inverse slope are indicated.
(F-G) DAmFRET plots of select “prion-like” low-complexity sequences (LCS) from yeast that were previously found to form non-amyloid aggregates (Psp1, Sla1) or non-prion amyloid (Ngr1), including a histogram of the Ngr1 LCS AmFRET values from the boxed gate, showing two populations of cells.

Figure 4. The archetypal prion domain, Sup35 PrD, forms non-prion condensates
(A) Stretched exponential fits of DAmFRET of Sup35 PrD in cells with different quinary structures of endogenous Rnq1, indicating inverse slopes.
(B) Corresponding DAmFRET plots of the curve fits shown in panel (A).
(C) Puncta morphologies of cells representative of boxes α and ß from panel (B), as seen by confocal microscopy at 63X magnification.
(D) Fluorescence recovery timescales of Sup35 PrD puncta as measured by FRAP.
(E) Single confocal slice showing two puncta (two arrows) coalescing into one punctum (single arrow) observed after an arbitrary time-point post induction. See also Fig. S4A.
(F) A montage of cells inducing Sup35 PrD showing the formation of liquid droplets stimulated by $NaAsO_2$ treatment (bottom) versus untreated cells (top). See also Fig. S4B.

Supplemental Figure 4. Related to Fig. 4
(A) Intensity (AU) of the two puncta (indicated by arrows in Fig. 4E at 0 min and 5 min) before and after coalescing with each other.
(B) Representative DAmFRET plots of [*pin*-] cells expressing Pub1 PrD, Sup35 PrD, Asc PYD and mEos3.1, upon treatment with $NaAsO_2$.

Figure 5. Sup35 PrD condensates are kinetically stable with respect to prion nucleation
(A) DAmFRET plots of prion-promoting or -inhibiting mutants of Sup35 PrD in cells with ([*PIN*+]) or without ([*pin*-]) endogenous Rnq1 amyloids. Red labels indicate the fraction of cells with a prion state as gated by the red box. Blue labels indicate the median AmFRET values for cells with high expression of the protein as indicated by the blue bracket. See also Fig. S5.
(B) A montage of a typical half FRAP experiment of a Sup35 PrD^Q punctum which shows no internal fluorescence recovery, indicative of a solid structure.
(C) DAmFRET plots of scrambled versions of Sup35 PrD in [*pin*-] and [*PIN*+] cells. Red and blue labels as in (A).
(D) A montage of a typical half FRAP experiment of a Sup35 PrD (#24) punctum showing no internal fluorescence recovery.

Supplemental Figure 5. Related to Fig. 5A
DAmFRET plots of Sup35 PrD and PrD^Q in cells with different endogenous amyloid templates ([*PIN*+], [*PSI*+ (Sc37)], or [*PSI*+ (Sc4)]). Blue labels as in Fig. 5A.

Figure 6. Quinary structure can kinetically control proteotoxicity
(A) [*pin*-] cells harboring plasmids encoding the indicated proteins were spotted as five-fold serial dilutions onto media that either induces (galactose) or represses (glucose) their expression.
(B) Budding indices were calculated among cells expressing Sup35 PrD #24 or unfused mEos3.1 to the same high level (5000 - 7000 AU). Solid bars denote [*pin*-], checkered bars [*PIN*+] cells. The latter is divided into high- and low-AmFRET subpopulations. Shown are means of five experiments; error bars represent 95 % CI. ****, $p<0.0001$ (ANOVA).

(C) DAmFRET plots of the indicated Rnq1 variants expressed in the absence (top) or presence (bottom) of endogenous Rnq1 amyloids.

Figure 7. Kinetic control of protein activity through quinary structure

(A) Schematic intracellular protein phase diagram for Sup35, with concentration on x-axis and oxidative stress on y-axis. The cell has crossed the liquid-solid phase boundary (dotted line) however endogenous Sup35 remains dispersed due to the large barrier to amyloid nucleation. Cells cross the liquid-liquid phase boundary (solid line) to form condensates either upon exposure to oxidative stress (represented by travel downward) or by forced over-expression (horizontal travel) as per the DAmFRET procedure.

(B) Schematic protein phase diagram indicating the boundary conditions for nucleated polymerization and condensation. Formally, every nucleated polymer isoform (e.g. amyloid "strain") will have its own phase boundary; for simplicity only one is shown. Nucleated protein polymers tend to be more stable than protein condensates; hence the phase space for nucleated polymerization encompasses that of condensation. Condensation is therefore metastable.

(C) Schematic of protein phase space that generalizes the findings of this paper. The phase diagram of (B) is projected along a third coordinate representing the nucleation barriers to polymerization and condensation. The barrier to amyloid nucleation depends only weakly on concentration, resulting in its intersection with that of condensation.

(D) The intersecting surfaces give rise to the phenomenon of two-step amyloid nucleation.

(E) Heterogenous templates (as for [*PIN*+] in the case of Sup35 PrD), or pre-folded globular subunits (as for death folds), reduce the conformational component of the nucleation barrier thereby allowing polymer nucleation to occur on observable timescales.

Bibliography

Adames, N.R., Schuck, P.L., Chen, K.C., Murali, T.M., Tyson, J.J., and Peccoud, J. (2015). Experimental testing of a new integrated model of the budding yeast Start transition. Mol Biol Cell *26*, 3966–3984.

Alberti, S., Halfmann, R., King, O., Kapila, A., and Lindquist, S. (2009). A systematic survey identifies prions and illuminates sequence features of prionogenic proteins. Cell *137*, 146–158.

Alberti, S., Halfmann, R., and Lindquist, S. (2010). Biochemical, Cell Biological, and Genetic Assays to Analyze Amyloid and Prion Aggregation in Yeast. In Guide to Yeast Genetics: Functional Genomics, Proteomics, and Other Systems Analysis, (Elsevier), pp. 709–734.

Auer, S., Ricchiuto, P., and Kashchiev, D. (2012). Two-step nucleation of amyloid fibrils: omnipresent or not? J Mol Biol *422*, 723–730.

Banani, S.F., Lee, H.O., Hyman, A.A., and Rosen, M.K. (2017). Biomolecular condensates: organizers of cellular biochemistry. Nat Rev Mol Cell Biol *18*, 285–298.

Basiji, D., and O'Gorman, M.R.G. (2015). Imaging flow cytometry. J Immunol Methods *423*, 1–2.

Bevington, P.R., and Robinson, D.K. (2003). Data reduction and error analysis for the physical sciences (McGraw-Hill).

Bondarev, S.A., Shchepachev, V.V., Kajava, A.V., and Zhouravleva, G.A. (2013). Effect of charged residues in the N-domain of Sup35 protein on prion [PSI+] stability and propagation. J Biol Chem *288*, 28503–28513.

Bradley, M.E., Edskes, H.K., Hong, J.Y., Wickner, R.B., and Liebman, S.W. (2002). Interactions among prions and prion "strains" in yeast. Proc Natl Acad Sci U S A *99 Suppl 4*, 16392–16399.

Bullitt, E., Rout, M.P., Kilmartin, J.V., and Akey, C.W. (1997). The yeast spindle pole body is assembled around a central crystal of Spc42p. Cell *89*, 1077–1086.

Cai, X., Chen, J., Xu, H., Liu, S., Jiang, Q.-X., Halfmann, R., and Chen, Z.J. (2014). Prion-like polymerization underlies signal transduction in antiviral immune defense and inflammasome activation. Cell *156*, 1207–1222.

Cascarina, S.M., and Ross, E.D. (2014). Yeast prions and human prion-like proteins: sequence features and prediction methods. Cell Mol Life Sci *71*, 2047–2063.

Caudron, F., and Barral, Y. (2013). A super-assembly of Whi3 encodes memory of deceptive encounters by single cells during yeast courtship. Cell *155*, 1244–1257.

Chakrabortee, S., Byers, J.S., Jones, S., Garcia, D.M., Bhullar, B., Chang, A., She, R., Lee, L., Fremin, B., Lindquist, S., et al. (2016a). Intrinsically disordered proteins drive emergence and inheritance of biological traits. Cell *167*, 369–381.e12.

Chakrabortee, S., Kayatekin, C., Newby, G.A., Mendillo, M.L., Lancaster, A., and Lindquist, S. (2016b). Luminidependens (LD) is an Arabidopsis protein with prion behavior. Proc Natl Acad Sci U S A *113*, 6065–6070.

Cheng, J., Waite, A.L., Tkaczyk, E.R., Ke, K., Richards, N., Hunt, A.J., and Gumucio, D.L. (2010). Kinetic properties of ASC protein aggregation in epithelial cells. J Cell Physiol *222*, 738–747.

Chernoff, Y.O. (2007). Stress and prions: lessons from the yeast model. FEBS Lett *581*, 3695–3701.

Chernoff, Y.O., Newnam, G.P., Kumar, J., Allen, K., and Zink, A.D. (1999). Evidence for a protein mutator in yeast: role of the Hsp70-related chaperone ssb in formation, stability, and toxicity of the [PSI] prion. Mol Cell Biol *19*, 8103–8112.

Daskalov, A., Paoletti, M., Ness, F., and Saupe, S.J. (2012). Genomic clustering and homology between HET-S and the NWD2 STAND protein in various fungal genomes. PLoS ONE *7*, e34854.

Daskalov, A., Gantner, M., Wälti, M.A., Schmidlin, T., Chi, C.N., Wasmer, C., Schütz, A., Ceschin, J., Clavé, C., Cescau, S., et al. (2014). Contribution of specific residues of the β-solenoid fold to HET-s prion function, amyloid structure and stability. PLoS Pathog *10*, e1004158.

Daskalov, A., Habenstein, B., Martinez, D., Debets, A.J.M., Sabaté, R., Loquet, A., and Saupe, S.J. (2015a). Signal transduction by a fungal NOD-like receptor based on propagation of a prion amyloid fold. PLoS Biol *13*, e1002059.

Daskalov, A., Dyrka, W., and Saupe, S.J. (2015b). Theme and variations: evolutionary diversification of the HET-s functional amyloid motif. Sci Rep *5*, 12494.

Derkatch, I.L., Bradley, M.E., Hong, J.Y., and Liebman, S.W. (2001). Prions affect the appearance of other prions: the story of [PIN(+)]. Cell *106*, 171–182.

Doronina, V.A., Staniforth, G.L., Speldewinde, S.H., Tuite, M.F., and Grant, C.M. (2015). Oxidative stress conditions increase the frequency of de novo formation of the yeast [PSI+] prion. Mol Microbiol *96*, 163–174.

Douglas, P.M., Treusch, S., Ren, H.-Y., Halfmann, R., Duennwald, M.L., Lindquist, S., and Cyr, D.M. (2008). Chaperone-dependent amyloid assembly protects cells from prion toxicity. Proc Natl Acad Sci U S A *105*, 7206–7211.

Du, Z., Park, K.-W., Yu, H., Fan, Q., and Li, L. (2008). Newly identified prion linked to the chromatin-remodeling factor Swi1 in Saccharomyces cerevisiae. Nat Genet *40*, 460–465.

Edelstein, S.J. (1980). Patterns in the quinary structures of proteins. Plasticity and inequivalence of individual molecules in helical arrays of sickle cell hemoglobin and tubulin. Biophys J *32*, 347–360.

Engler, C., and Marillonnet, S. (2013). Combinatorial DNA assembly using Golden Gate cloning. Methods Mol Biol *1073*, 141–156.

Falahati, H., and Wieschaus, E. (2017). Independent active and thermodynamic processes govern the nucleolus assembly in vivo. Proc Natl Acad Sci U S A *114*, 1335–1340.

Ferreira, P.C., Ness, F., Edwards, S.R., Cox, B.S., and Tuite, M.F. (2001). The elimination of the yeast [PSI+] prion by guanidine hydrochloride is the result of Hsp104 inactivation. Mol Microbiol *40*, 1357–1369.

Futcher, A.B., and Cox, B.S. (1984). Copy number and the stability of 2-micron circle-based artificial plasmids of Saccharomyces cerevisiae. J Bacteriol *157*, 283–290.

Garcia, D.M., Dietrich, D., Clardy, J., and Jarosz, D.F. (2016). A common bacterial metabolite elicits prion-based bypass of glucose repression. Elife *5*.

Garcia-Seisdedos, H., Empereur-Mot, C., Elad, N., and Levy, E.D. (2017). Proteins evolve on the edge of supramolecular self-assembly. Nature *548*, 244–247.

Gendoo, D.M.A., and Harrison, P.M. (2011). Origins and evolution of the HET-s prion-forming protein: searching for other amyloid-forming solenoids. PLoS ONE *6*, e27342.

Gietz, D., St Jean, A., Woods, R.A., and Schiestl, R.H. (1992). Improved method for high efficiency transformation of intact yeast cells. Nucleic Acids Res *20*, 1425.

Gilks, N., Kedersha, N., Ayodele, M., Shen, L., Stoecklin, G., Dember, L.M., and Anderson, P. (2004). Stress granule assembly is mediated by prion-like aggregation of TIA-1. Mol Biol Cell *15*, 5383–5398.

Glover, J.R., Kowal, A.S., Schirmer, E.C., Patino, M.M., Liu, J.J., and Lindquist, S. (1997). Self-seeded fibers formed by Sup35, the protein determinant of [PSI+], a heritable prion-like factor of S. cerevisiae. Cell *89*, 811–819.

Goldschmidt, L., Teng, P.K., Riek, R., and Eisenberg, D. (2010). Identifying the amylome, proteins capable of forming amyloid-like fibrils. Proc Natl Acad Sci U S A *107*, 3487–3492.

Goldstein, A.L., and McCusker, J.H. (1999). Three new dominant drug resistance cassettes for gene disruption in Saccharomyces cerevisiae. Yeast.

Grassmann, A., Wolf, H., Hofmann, J., Graham, J., and Vorberg, I. (2013). Cellular aspects of prion replication in vitro. Viruses *5*, 374–405.

Halfmann, R. (2016). A glass menagerie of low complexity sequences. Current Opinion in Structural Biology *38*, 9–16.

Halfmann, R., and Lindquist, S. (2010). Epigenetics in the extreme: prions and the inheritance of environmentally acquired traits. Science *330*, 629–632.

Halfmann, R., Alberti, S., Krishnan, R., Lyle, N., O'Donnell, C.W., King, O.D., Berger, B., Pappu, R.V., and Lindquist, S. (2011). Opposing effects of glutamine and asparagine govern prion formation by intrinsically disordered proteins. Mol Cell *43*, 72–84.

Halfmann, R., Jarosz, D.F., Jones, S.K., Chang, A., Lancaster, A.K., and Lindquist, S. (2012). Prions are a common mechanism for phenotypic inheritance in wild yeasts. Nature *482*, 363–368.

Hastings, P.J., McGill, C., Shafer, B., and Strathern, J.N. (1993). Ends-in vs. ends-out recombination in yeast. Genetics *135*, 973–980.

Holmes, D.L., Lancaster, A.K., Lindquist, S., and Halfmann, R. (2013). Heritable remodeling of yeast multicellularity by an environmentally responsive prion. Cell *153*, 153–165.

Jares-Erijman, E.A., and Jovin, T.M. (2003). FRET imaging. Nat Biotechnol *21*, 1387–1395.

Kabani, M., and Melki, R. (2015). Sup35p in Its Soluble and Prion States Is Packaged inside Extracellular Vesicles. MBio *6*.

Kajava, A.V., Klopffleisch, K., Chen, S., and Hofmann, K. (2014). Evolutionary link between metazoan RHIM motif and prion-forming domain of fungal heterokaryon incompatibility factor HET-s/HET-s. Sci Rep *4*, 7436.

Kashchiev, D. (2015). Protein Polymerization into Fibrils from the Viewpoint of Nucleation Theory. Biophys J *109*, 2126–2136.

Kashchiev, D., and Auer, S. (2010). Nucleation of amyloid fibrils. J Chem Phys *132*, 215101.

King, C.-Y., and Diaz-Avalos, R. (2004). Protein-only transmission of three yeast prion strains. Nature *428*, 319–323.

Knowles, T.P.J., Vendruscolo, M., and Dobson, C.M. (2014). The amyloid state and its association with protein misfolding diseases. Nat Rev Mol Cell Biol *15*, 384–396.

Kroschwald, S., Maharana, S., Mateju, D., Malinovska, L., Nüske, E., Poser, I., Richter, D., and Alberti, S. (2015). Promiscuous interactions and protein disaggregases determine the material state of stress-inducible RNP granules. Elife *4*, e06807.

Lancaster, A.K., Bardill, J.P., True, H.L., and Masel, J. (2010). The spontaneous appearance rate of the yeast prion [PSI+] and its implications for the evolution of the evolvability properties of the [PSI+] system. Genetics *184*, 393–400.

Li, J., McQuade, T., Siemer, A.B., Napetschnig, J., Moriwaki, K., Hsiao, Y.-S., Damko, E., Moquin, D., Walz, T., McDermott, A., et al. (2012). The RIP1/RIP3 necrosome forms a functional amyloid signaling complex required for programmed necrosis. Cell *150*, 339–350.

Li, X., Rayman, J.B., Kandel, E.R., and Derkatch, I.L. (2014). Functional role of Tia1/Pub1 and Sup35 prion domains: directing protein synthesis machinery to the tubulin cytoskeleton. Mol Cell *55*, 305–318.

Liebman, S.W., and Chernoff, Y.O. (2012). Prions in yeast. Genetics *191*, 1041–1072.

Lin, Y., Protter, D.S.W., Rosen, M.K., and Parker, R. (2015). Formation and Maturation of Phase-Separated Liquid Droplets by RNA-Binding Proteins. Mol Cell *60*, 208–219.

Loison, G., Vidal, A., Findeli, A., Roitsch, C., Balloul, J.M., and Lemoine, Y. (1989). High level of expression of a protective antigen of schistosomes in Saccharomyces cerevisiae. Yeast *5*, 497–507.

Lu, A., Magupalli, V.G., Ruan, J., Yin, Q., Atianand, M.K., Vos, M.R., Schröder, G.F., Fitzgerald, K.A., Wu, H., and Egelman, E.H. (2014). Unified polymerization mechanism for the assembly of

ASC-dependent inflammasomes. Cell *156*, 1193–1206.

Lyle, J.M., Bullitt, E., Bienz, K., and Kirkegaard, K. (2002). Visualization and functional analysis of RNA-dependent RNA polymerase lattices. Science *296*, 2218–2222.

Marzahn, M.R., Marada, S., Lee, J., Nourse, A., Kenrick, S., Zhao, H., Ben-Nissan, G., Kolaitis, R.-M., Peters, J.L., Pounds, S., et al. (2016). Higher-order oligomerization promotes localization of SPOP to liquid nuclear speckles. EMBO J *35*, 1254–1275.

Maurer-Stroh, S., Debulpaep, M., Kuemmerer, N., Lopez de la Paz, M., Martins, I.C., Reumers, J., Morris, K.L., Copland, A., Serpell, L., Serrano, L., et al. (2010). Exploring the sequence determinants of amyloid structure using position-specific scoring matrices. Nat Methods *7*, 237–242.

McGlinchey, R.P., Kryndushkin, D., and Wickner, R.B. (2011). Suicidal [PSI+] is a lethal yeast prion. Proc Natl Acad Sci U S A *108*, 5337–5341.

Michaels, T.C.T., Liu, L.X., Meisl, G., and Knowles, T.P.J. (2017). Physical principles of filamentous protein self-assembly kinetics. J Phys Condens Matter *29*, 153002.

Molliex, A., Temirov, J., Lee, J., Coughlin, M., Kanagaraj, A.P., Kim, H.J., Mittag, T., and Taylor, J.P. (2015). Phase separation by low complexity domains promotes stress granule assembly and drives pathological fibrillization. Cell *163*, 123–133.

Müller, J.D. (2004). Cumulant analysis in fluorescence fluctuation spectroscopy. Biophys J *86*, 3981–3992.

Nakayashiki, T., Kurtzman, C.P., Edskes, H.K., and Wickner, R.B. (2005). Yeast prions [URE3] and [PSI+] are diseases. Proc Natl Acad Sci U S A *102*, 10575–10580.

Nelson, R., Sawaya, M.R., Balbirnie, M., Madsen, A.Ø., Riekel, C., Grothe, R., and Eisenberg, D. (2005). Structure of the cross-beta spine of amyloid-like fibrils. Nature *435*, 773–778.

Patel, B.K., Gavin-Smyth, J., and Liebman, S.W. (2009). The yeast global transcriptional co-repressor protein Cyc8 can propagate as a prion. Nat Cell Biol *11*, 344–349.

Petrovska, I., Nüske, E., Munder, M.C., Kulasegaran, G., Malinovska, L., Kroschwald, S., Richter, D., Fahmy, K., Gibson, K., Verbavatz, J.-M., et al. (2014). Filament formation by metabolic enzymes is a specific adaptation to an advanced state of cellular starvation. Elife *3*.

Riback, J.A., Katanski, C.D., Kear-Scott, J.L., Pilipenko, E.V., Rojek, A.E., Sosnick, T.R., and Drummond, D.A. (2017). Stress-Triggered Phase Separation Is an Adaptive, Evolutionarily Tuned Response. Cell *168*, 1028–1040.e19.

Ross, E.D., Edskes, H.K., Terry, M.J., and Wickner, R.B. (2005). Primary sequence independence for prion formation. Proc Natl Acad Sci U S A *102*, 12825–12830.

Saad, S., Cereghetti, G., Feng, Y., Picotti, P., Peter, M., and Dechant, R. (2017). Reversible protein aggregation is a protective mechanism to ensure cell cycle restart after stress. Nat Cell Biol *19*, 1202–1213.

Satpute-Krishnan, P., and Serio, T.R. (2005). Prion protein remodelling confers an immediate phenotypic switch. Nature *437*, 262–265.

Schmitz, A.M., Morrison, M.F., Agunwamba, A.O., Nibert, M.L., and Lesser, C.F. (2009). Protein interaction platforms: visualization of interacting proteins in yeast. Nat Methods *6*, 500–502.

Serio, T.R., Cashikar, A.G., Kowal, A.S., Sawicki, G.J., Moslehi, J.J., Serpell, L., Arnsdorf, M.F., and Lindquist, S.L. (2000). Nucleated conformational conversion and the replication of conformational information by a prion determinant. Science *289*, 1317–1321.

Seuring, C., Greenwald, J., Wasmer, C., Wepf, R., Saupe, S.J., Meier, B.H., and Riek, R. (2012). The mechanism of toxicity in HET-S/HET-s prion incompatibility. PLoS Biol *10*, e1001451.

Shivaraju, M., Unruh, J.R., Slaughter, B.D., Mattingly, M., Berman, J., and Gerton, J.L. (2012). Cell-cycle-coupled structural oscillation of centromeric nucleosomes in yeast. Cell *150*, 304–316.

Si, K., and Kandel, E.R. (2016). The Role of Functional Prion-Like Proteins in the Persistence of Memory. Cold Spring Harb Perspect Biol *8*, a021774.

Si, K., Lindquist, S., and Kandel, E.R. (2003). A neuronal isoform of the aplysia CPEB has prion-like properties. Cell *115*, 879–891.

Slaughter, B.D., Unruh, J.R., and Li, R. (2011). Fluorescence fluctuation spectroscopy and imaging methods for examination of dynamic protein interactions in yeast. Methods Mol Biol *759*, 283–306.

Sondheimer, N., and Lindquist, S. (2000). Rnq1: an epigenetic modifier of protein function in yeast. Mol Cell *5*, 163–172.

Sun, Y., Leong, N.T., Wong, T., and Drubin, D.G. (2015). A Pan1/End3/Sla1 complex links Arp2/3-mediated actin assembly to sites of clathrin-mediated endocytosis. Mol Biol Cell *26*, 3841–3856.

Suzuki, G., Shimazu, N., and Tanaka, M. (2012). A yeast prion, Mod5, promotes acquired drug resistance and cell survival under environmental stress. Science *336*, 355–359.

Tanaka, M., Collins, S.R., Toyama, B.H., and Weissman, J.S. (2006). The physical basis of how prion conformations determine strain phenotypes. Nature *442*, 585–589.

Tang, E.D., and Wang, C.-Y. (2009). MAVS self-association mediates antiviral innate immune signaling. J Virol *83*, 3420–3428.

Tong, A.H.Y., and Boone, C. (2007). 16 High-Throughput Strain Construction and Systematic Synthetic Lethal Screening in. In Yeast Gene Analysis - Second Edition, (Elsevier), pp. 369–707.

Treusch, S., and Lindquist, S. (2012). An intrinsically disordered yeast prion arrests the cell cycle by sequestering a spindle pole body component. J Cell Biol *197*, 369–379.

Tycko, R., and Wickner, R.B. (2013). Molecular structures of amyloid and prion fibrils:

consensus versus controversy. Acc Chem Res *46*, 1487–1496.

Tyedmers, J., Madariaga, M.L., and Lindquist, S. (2008). Prion switching in response to environmental stress. PLoS Biol *6*, e294.

Uchida, M., Sun, Y., McDermott, G., Knoechel, C., Le Gros, M.A., Parkinson, D., Drubin, D.G., and Larabell, C.A. (2011). Quantitative analysis of yeast internal architecture using soft X-ray tomography. Yeast *28*, 227–236.

Urakov, V.N., Vishnevskaya, A.B., Alexandrov, I.M., Kushnirov, V.V., Smirnov, V.N., and Ter-Avanesyan, M.D. (2010). Interdependence of amyloid formation in yeast: implications for polyglutamine disorders and biological functions. Prion *4*, 45–52.

Vaĭnshteĭn, B.K. (1973). Three-dimensional electron microscopy of biological macromolecules. Sov. Phys. Usp. *16*, 185–206.

Vekilov, P.G. (2012). Phase diagrams and kinetics of phase transitions in protein solutions. J Phys Condens Matter *24*, 193101.

Wallace, E.W.J., Kear-Scott, J.L., Pilipenko, E.V., Schwartz, M.H., Laskowski, P.R., Rojek, A.E., Katanski, C.D., Riback, J.A., Dion, M.F., Franks, A.M., et al. (2015). Reversible, Specific, Active Aggregates of Endogenous Proteins Assemble upon Heat Stress. Cell *162*, 1286–1298.

Wan, W., and Stubbs, G. (2014). Fungal prion HET-s as a model for structural complexity and self-propagation in prions. Proc Natl Acad Sci U S A *111*, 5201–5206.

Wasmer, C., Lange, A., Van Melckebeke, H., Siemer, A.B., Riek, R., and Meier, B.H. (2008). Amyloid fibrils of the HET-s(218-289) prion form a beta solenoid with a triangular hydrophobic core. Science *319*, 1523–1526.

Wickner, R.B. (1994). [URE3] as an altered URE2 protein: evidence for a prion analog in Saccharomyces cerevisiae. Science *264*, 566–569.

Wiedenmann, J., Ivanchenko, S., Oswald, F., Schmitt, F., Röcker, C., Salih, A., Spindler, K.-D., and Nienhaus, G.U. (2004). EosFP, a fluorescent marker protein with UV-inducible green-to-red fluorescence conversion. Proc Natl Acad Sci U S A *101*, 15905–15910.

ten Wolde, P.R., and Frenkel, D. (1997). Enhancement of protein crystal nucleation by critical density fluctuations. Science *277*, 1975–1978.

Wu, H., and Fuxreiter, M. (2016). The Structure and Dynamics of Higher-Order Assemblies: Amyloids, Signalosomes, and Granules. Cell *165*, 1055–1066.

Wu, B., Peisley, A., Tetrault, D., Li, Z., Egelman, E.H., Magor, K.E., Walz, T., Penczek, P.A., and Hur, S. (2014). Molecular imprinting as a signal-activation mechanism of the viral RNA sensor RIG-I. Mol Cell *55*, 511–523.

Xu, H., He, X., Zheng, H., Huang, L.J., Hou, F., Yu, Z., de la Cruz, M.J., Borkowski, B., Zhang, X., Chen, Z.J., et al. (2015). Correction: Structural basis for the prion-like MAVS filaments in antiviral innate immunity. Elife *4*.

Yuan, A.H., and Hochschild, A. (2017). A bacterial global regulator forms a prion. Science *355*, 198–201.

Zhang, L., and Schmit, J.D. (2016). Pseudo-one-dimensional nucleation in dilute polymer solutions. Phys Rev E *93*, 060401.

Zhang, M., Chang, H., Zhang, Y., Yu, J., Wu, L., Ji, W., Chen, J., Liu, B., Lu, J., Liu, Y., et al. (2012). Rational design of true monomeric and bright photoactivatable fluorescent proteins. Nat Methods *9*, 727–729.

Zhang, X.-F., Sun, R., Guo, Q., Zhang, S., Meulia, T., Halfmann, R., Li, D., and Qu, F. (2017). A self-perpetuating repressive state of a viral replication protein blocks superinfection by the same virus. PLoS Pathog *13*, e1006253.

Zhao, D., and Moore, J.S. (2003). Nucleation-elongation: a mechanism for cooperative supramolecular polymerization. Org Biomol Chem *1*, 3471–3491.

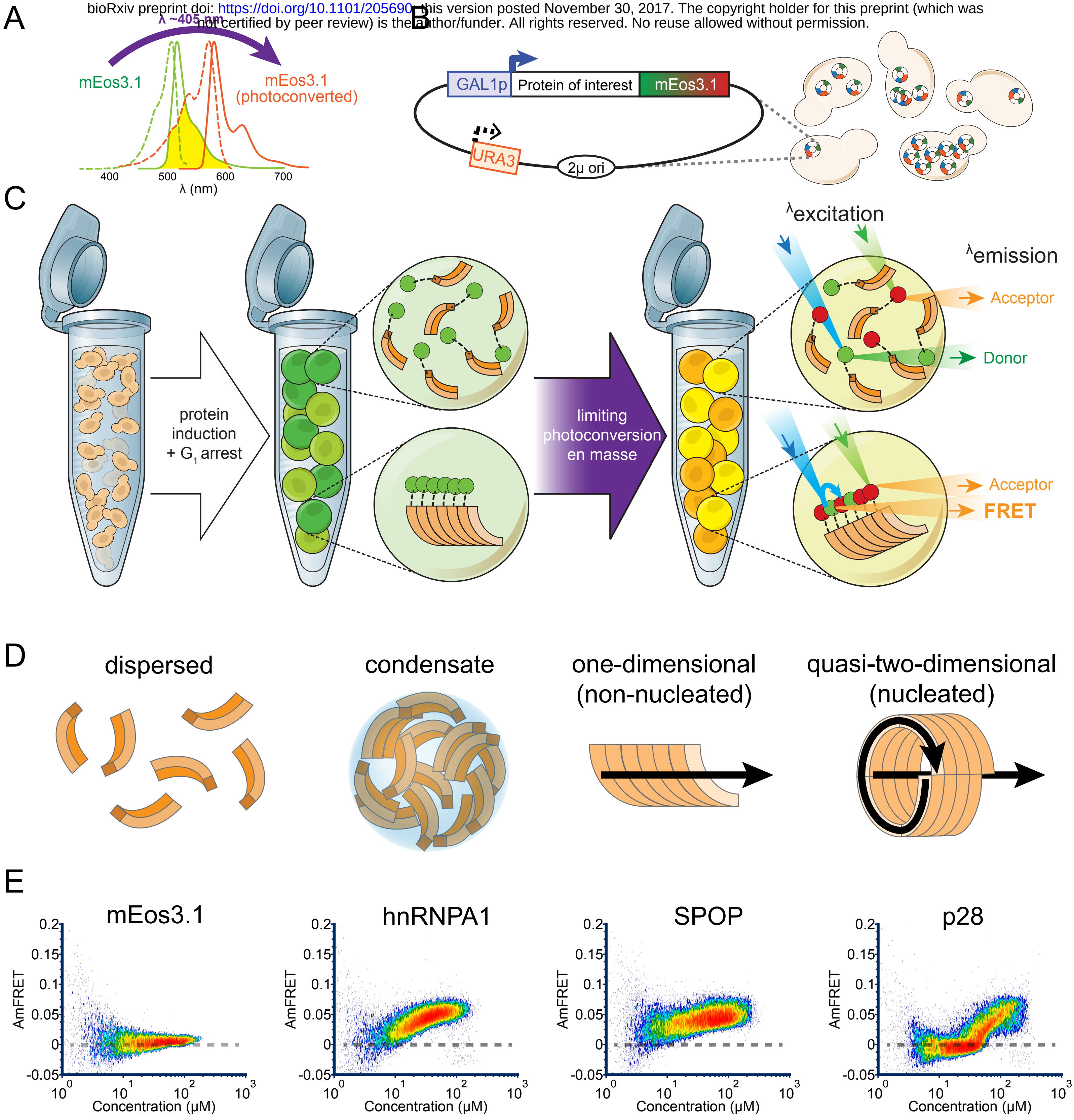
A
λ ~405 nm
mEos3.1
mEos3.1
(photoconverted)
400
500
600
700
λ (nm)
B
GAL1p
Protein of interest
mEos3.1
URA3
2μ ori
C
protein
induction
+ G1 arrest
limiting
photoconversion
en masse
λexcitation
λemission
Acceptor
Donor
Acceptor
FRET
D
dispersed
condensate
one-dimensional
(non-nucleated)
quasi-two-dimensional
(nucleated)
E
mEos3.1
hnRNPA1
SPOP
p28
AmFRET
0.2
0.15
0.1
0.05
0
-0.05
10^0
10^1
10^2
10^3
Concentration (μM)

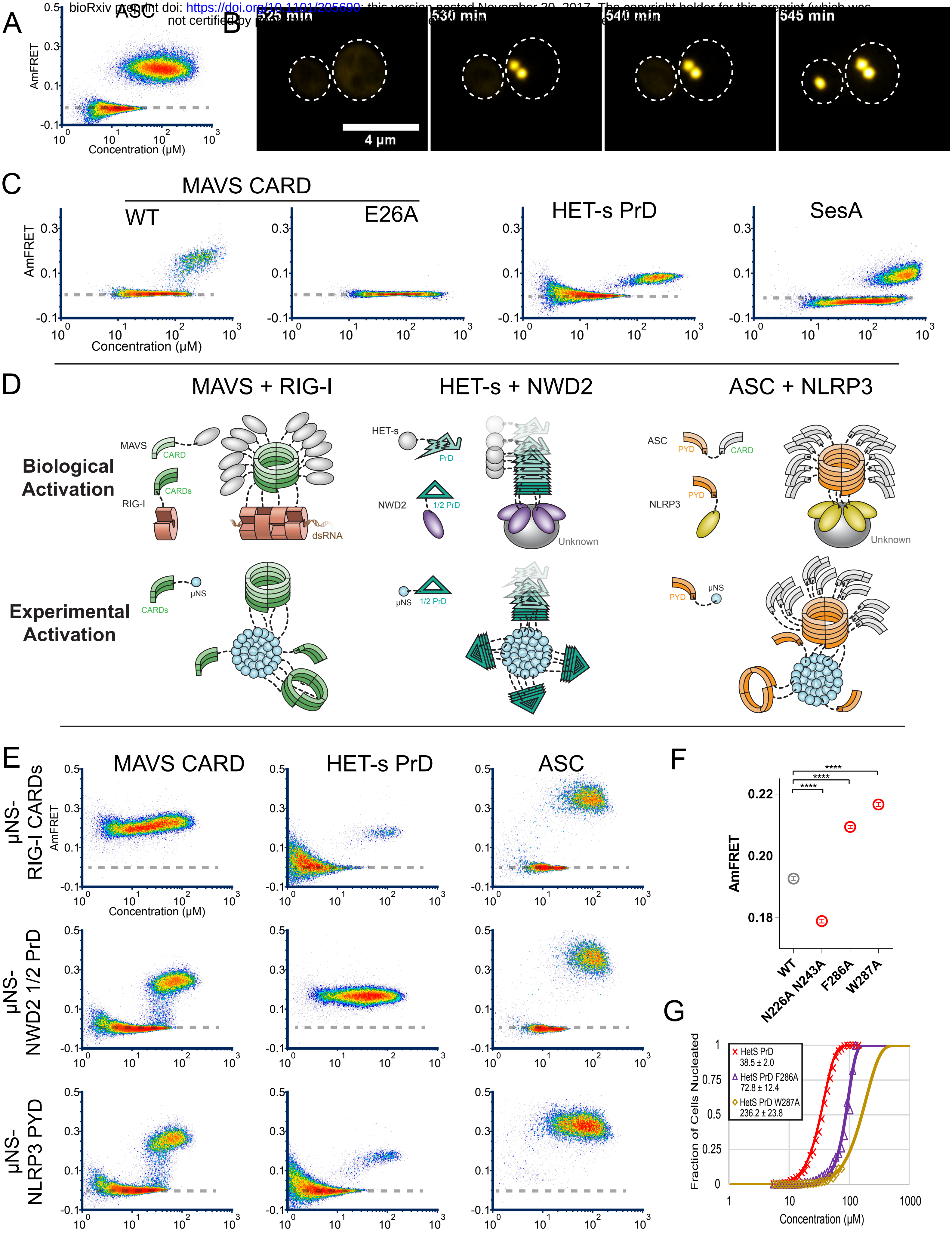
A
ASC
AmFRET
Concentration (μM)
B
525 min
530 min
540 min
545 min
4 μm
C
MAVS CARD
WT
E26A
HET-s PrD
SesA
AmFRET
Concentration (μM)
D
MAVS + RIG-I
HET-s + NWD2
ASC + NLRP3
Biological Activation
MAVS
CARD
RIG-I
CARDs
dsRNA
HET-s
PrD
NWD2
1/2 PrD
Unknown
ASC
PYD
CARD
NLRP3
PYD
Unknown
Experimental Activation
CARDs
μNS
μNS
1/2 PrD
PYD
μNS
E
MAVS CARD
HET-s PrD
ASC
μNS-RIG-I CARDs
μNS-NWD2 1/2 PrD
μNS-NLRP3 PYD
AmFRET
Concentration (μM)
F
AmFRET
****
****
****
0.22
0.20
0.18
WT
N226A N243A
F286A
W287A
G
Fraction of Cells Nucleated
HetS PrD 38.5 ± 2.0
HetS PrD F286A 72.8 ± 12.4
HetS PrD W287A 236.2 ± 23.8
Concentration (μM)
1
10
100
1000
0
0.25
0.5
0.75
1

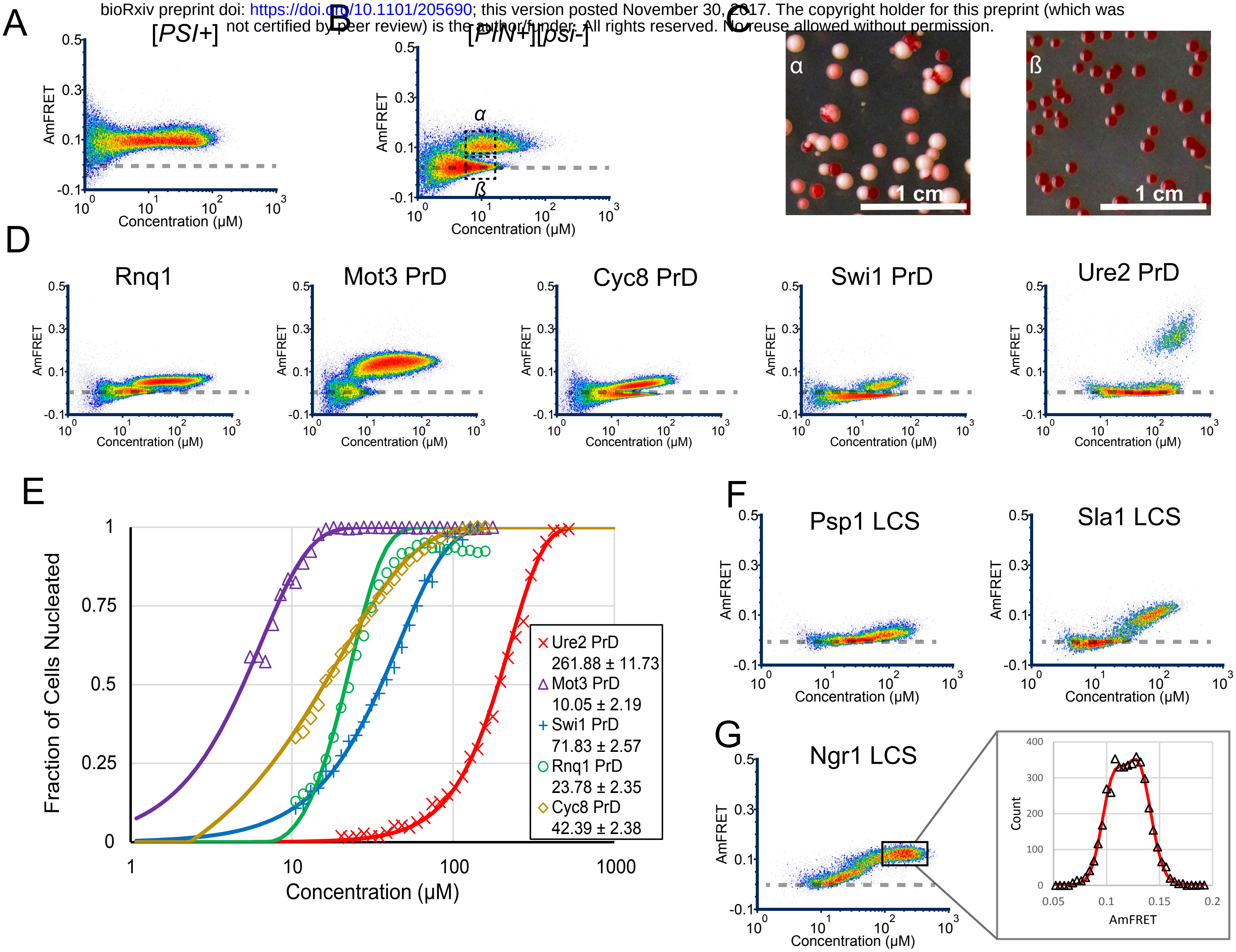
A
[PSI+]
AmFRET
Concentration (μM)
B
[PIN+][psi-]
α
ß
C
α
ß
1 cm
1 cm
D
Rnq1
Mot3 PrD
Cyc8 PrD
Swi1 PrD
Ure2 PrD
E
Fraction of Cells Nucleated
Concentration (μM)
Ure2 PrD 261.88 ± 11.73
Mot3 PrD 10.05 ± 2.19
Swi1 PrD 71.83 ± 2.57
Rnq1 PrD 23.78 ± 2.35
Cyc8 PrD 42.39 ± 2.38
F
Psp1 LCS
Sla1 LCS
G
Ngr1 LCS
Count
AmFRET

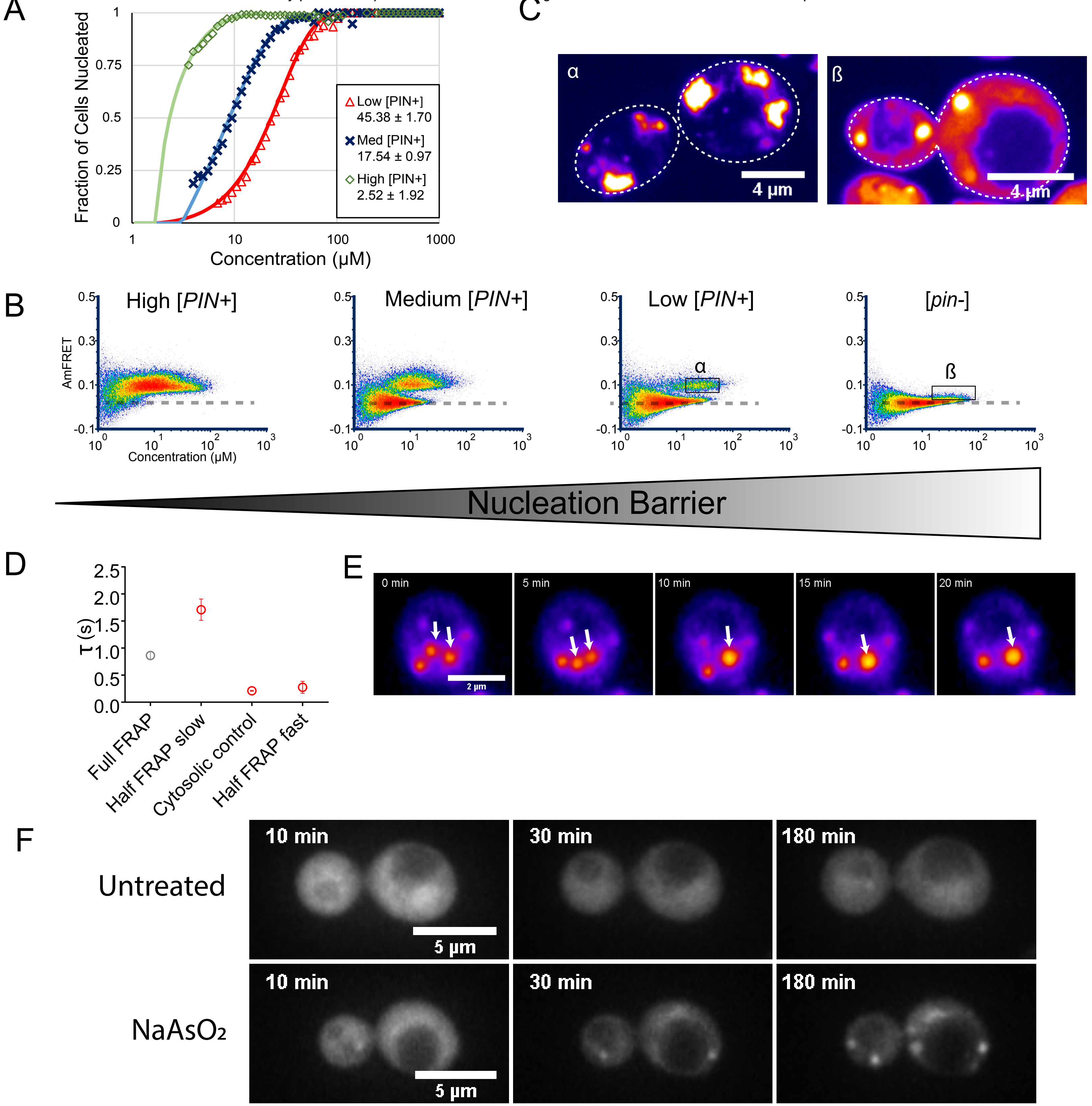
A
Fraction of Cells Nucleated
1
0.75
0.5
0.25
0
1
10
100
1000
Concentration (μM)
△ Low [PIN+] 45.38 ± 1.70
✕ Med [PIN+] 17.54 ± 0.97
◇ High [PIN+] 2.52 ± 1.92
C
α
ß
4 μm
4 μm
B
High [PIN+]
Medium [PIN+]
Low [PIN+]
[pin-]
AmFRET
0.5
0.3
0.1
-0.1
10^0
10^1
10^2
10^3
Concentration (μM)
α
ß
Nucleation Barrier
D
τ (s)
2.5
2.0
1.5
1.0
0.5
0.0
Full FRAP
Half FRAP slow
Cytosolic control
Half FRAP fast
E
0 min
5 min
10 min
15 min
20 min
2 μm
F
Untreated
NaAsO₂
10 min
30 min
180 min
5 μm

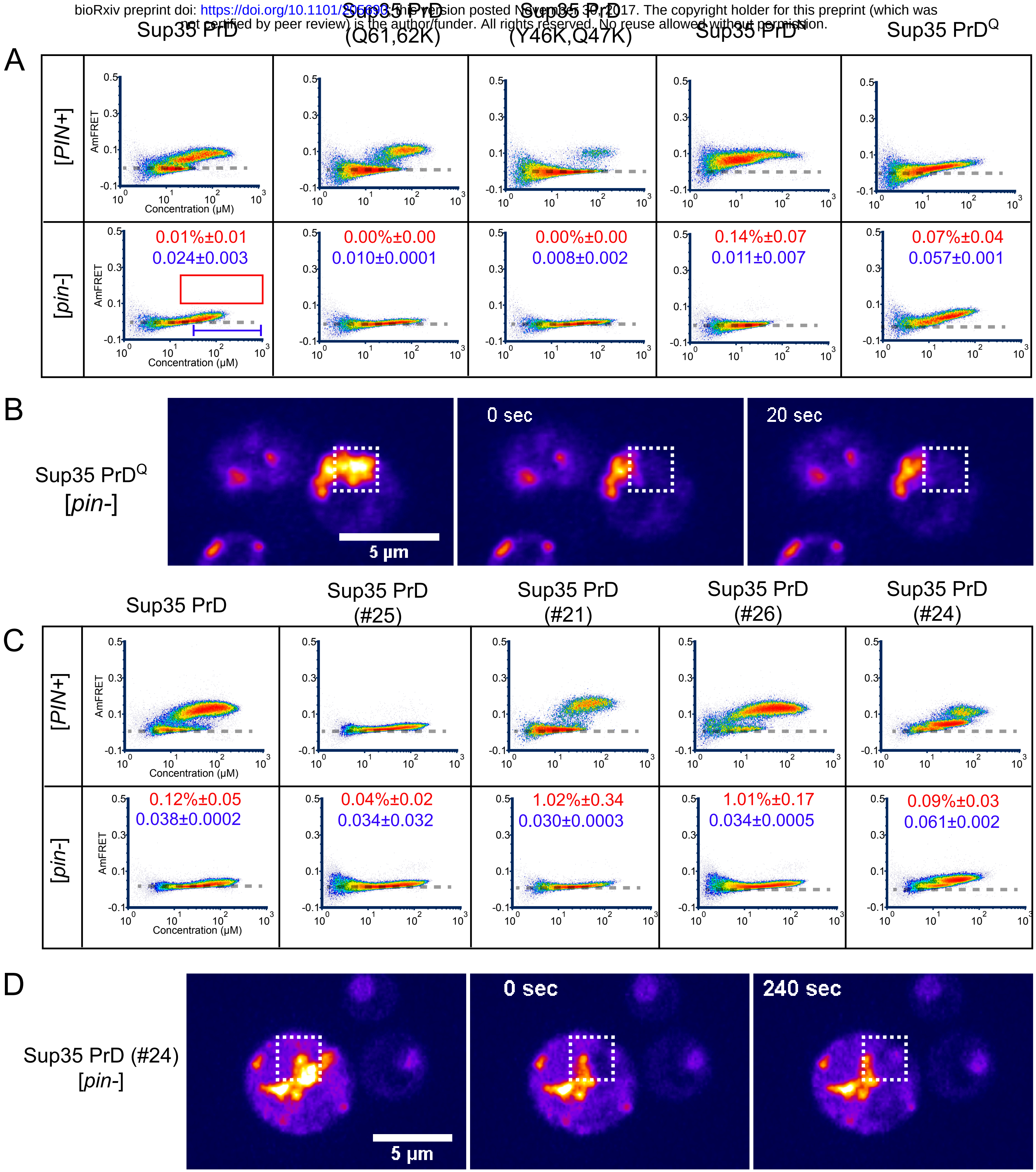
A
Sup35 PrD
Sup35 PrD (Q61,62K)
Sup35 PrD (Y46K,Q47K)
Sup35 PrD^N
Sup35 PrD^Q
[PIN+]
[pin-]
AmFRET
Concentration (µM)
0.01%±0.01
0.024±0.003
0.00%±0.00
0.010±0.0001
0.00%±0.00
0.008±0.002
0.14%±0.07
0.011±0.007
0.07%±0.04
0.057±0.001
B
Sup35 PrD^Q
[pin-]
0 sec
20 sec
5 µm
C
Sup35 PrD
Sup35 PrD (#25)
Sup35 PrD (#21)
Sup35 PrD (#26)
Sup35 PrD (#24)
[PIN+]
[pin-]
AmFRET
Concentration (µM)
0.12%±0.05
0.038±0.0002
0.04%±0.02
0.034±0.032
1.02%±0.34
0.030±0.0003
1.01%±0.17
0.034±0.0005
0.09%±0.03
0.061±0.002
D
Sup35 PrD (#24)
[pin-]
0 sec
240 sec
5 µm

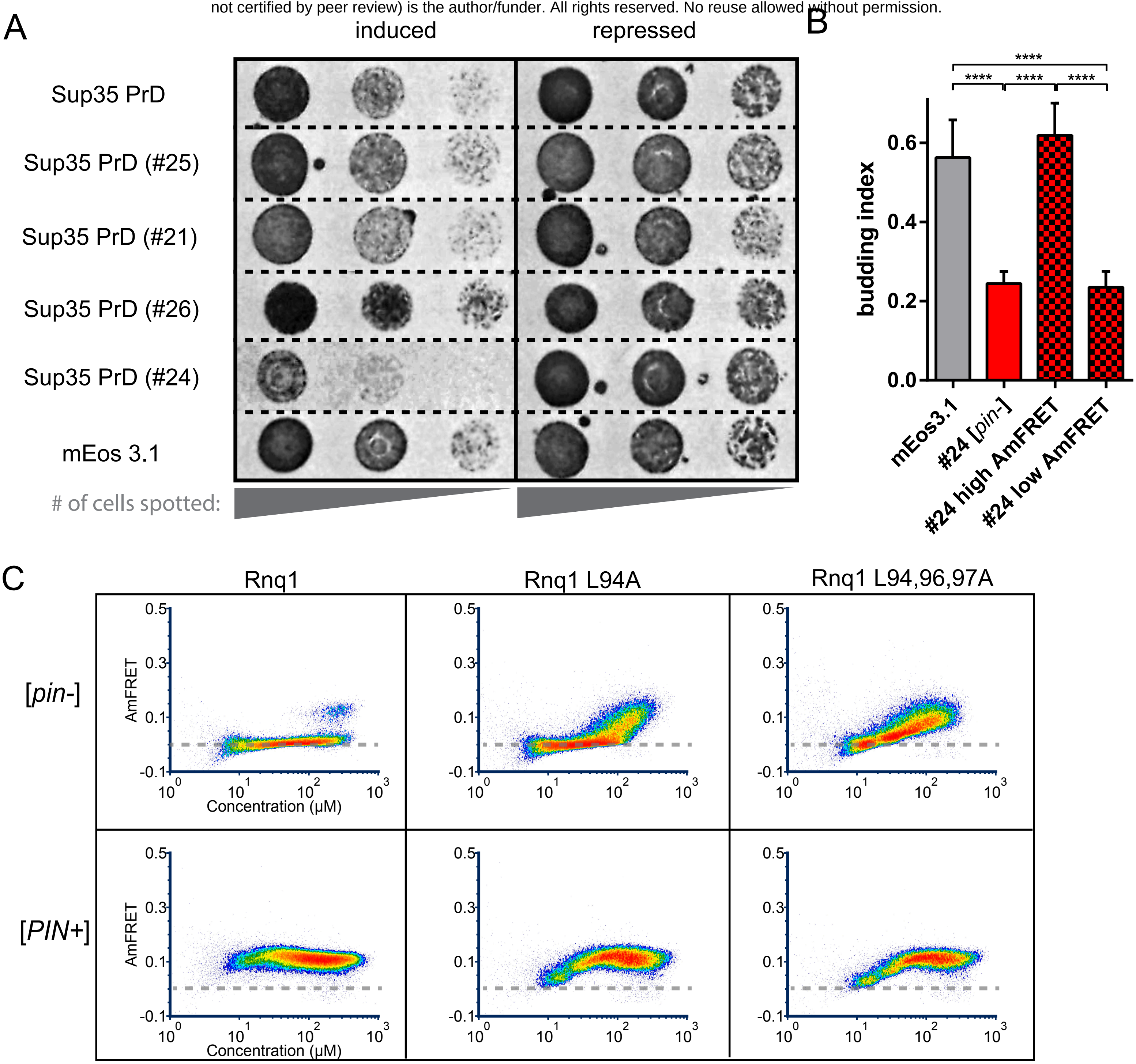
A
induced
repressed
Sup35 PrD
Sup35 PrD (#25)
Sup35 PrD (#21)
Sup35 PrD (#26)
Sup35 PrD (#24)
mEos 3.1
# of cells spotted:
B
****
****
****
****
budding index
0.0
0.2
0.4
0.6
mEos3.1
#24 [pin-]
#24 high AmFRET
#24 low AmFRET
C
Rnq1
Rnq1 L94A
Rnq1 L94,96,97A
[pin-]
[PIN+]
AmFRET
0.5
0.3
0.1
-0.1
10^0
10^1
10^2
10^3
Concentration (μM)

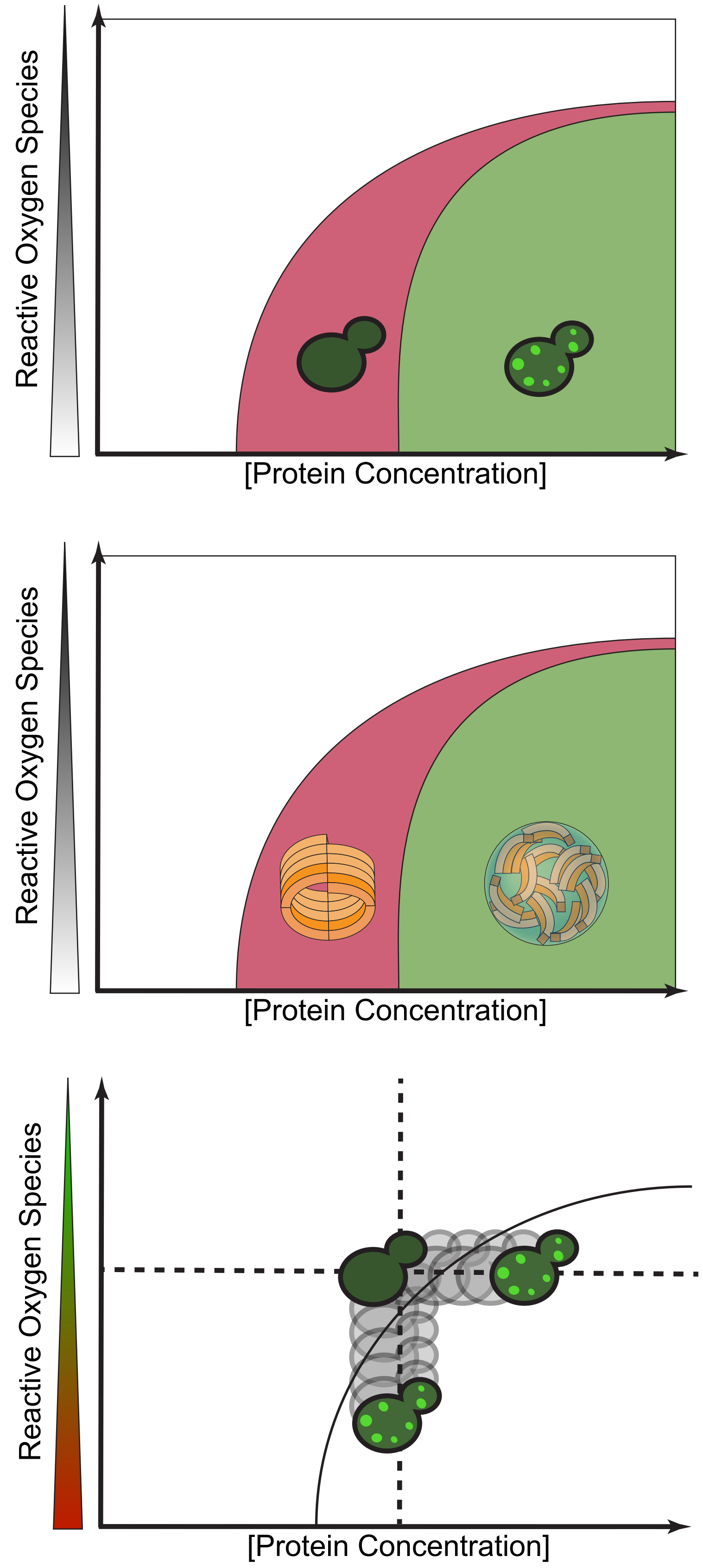
Reactive Oxygen Species
[Protein Concentration]
Reactive Oxygen Species
[Protein Concentration]
Reactive Oxygen Species
[Protein Concentration]

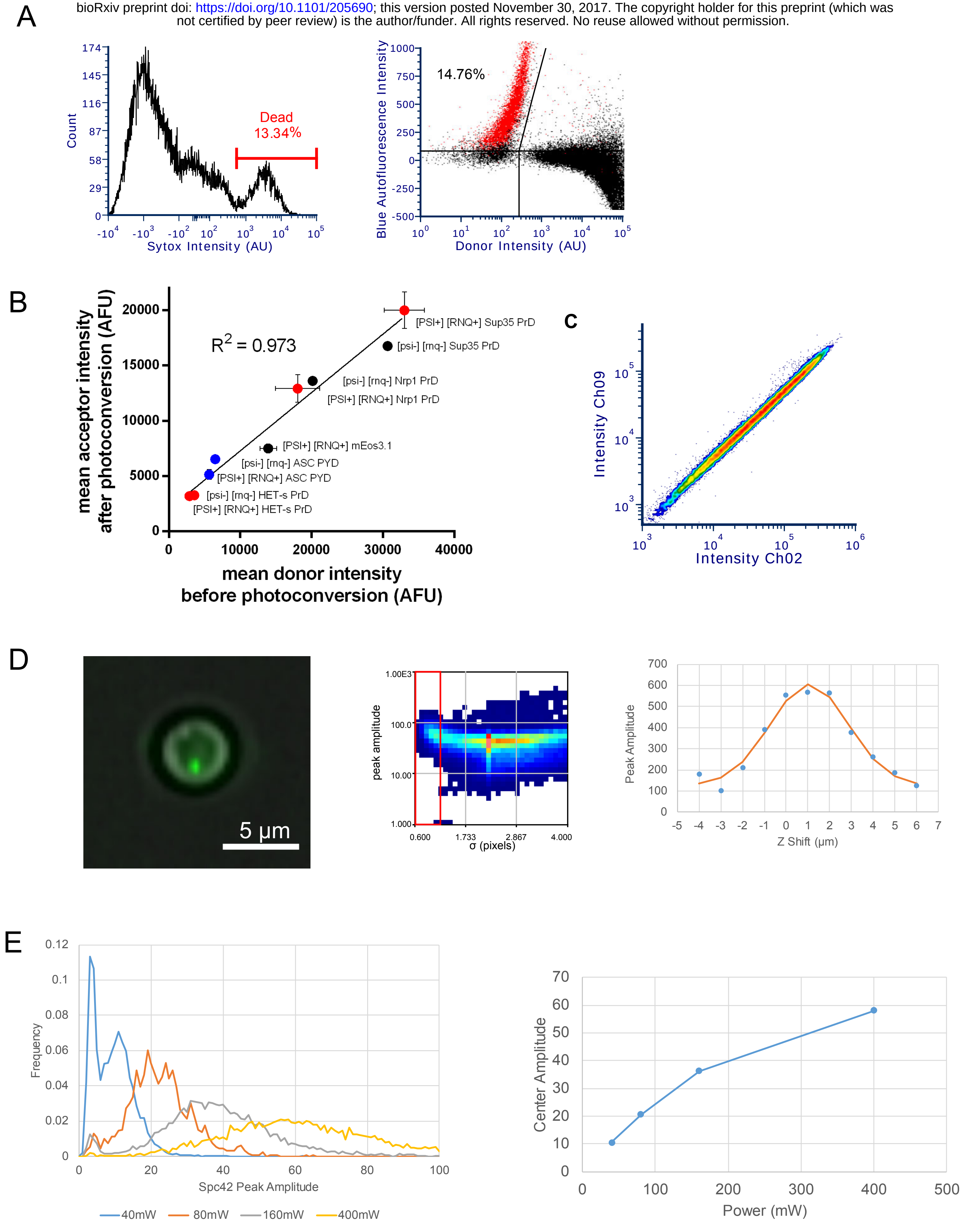
A
Count
174
145
116
87
58
29
0
Dead
13.34%
-10^4 -10^3 -10^2 10^2 10^3 10^4 10^5
Sytox Intensity (AU)
Blue Autofluorescence Intensity
1000
750
500
250
0
-250
-500
14.76%
10^0 10^1 10^2 10^3 10^4 10^5
Donor Intensity (AU)
B
mean acceptor intensity after photoconversion (AFU)
20000
15000
10000
5000
0
R^2 = 0.973
[PSI+] [RNQ+] Sup35 PrD
[psi-] [rnq-] Sup35 PrD
[psi-] [rnq-] Nrp1 PrD
[PSI+] [RNQ+] Nrp1 PrD
[PSI+] [RNQ+] mEos3.1
[psi-] [rnq-] ASC PYD
[PSI+] [RNQ+] ASC PYD
[psi-] [rnq-] HET-s PrD
[PSI+] [RNQ+] HET-s PrD
0
10000
20000
30000
40000
mean donor intensity before photoconversion (AFU)
C
Intensity Ch09
10^5
10^4
10^3
10^3 10^4 10^5 10^6
Intensity Ch02
D
5 µm
1.00E3
100.0
10.00
1.000
peak amplitude
0.600
1.733
2.867
4.000
σ (pixels)
Peak Amplitude
700
600
500
400
300
200
100
0
-5 -4 -3 -2 -1 0 1 2 3 4 5 6 7
Z Shift (µm)
E
Frequency
0.12
0.1
0.08
0.06
0.04
0.02
0
0
20
40
60
80
100
Spc42 Peak Amplitude
40mW
80mW
160mW
400mW
Center Amplitude
70
60
50
40
30
20
10
0
0
100
200
300
400
500
Power (mW)

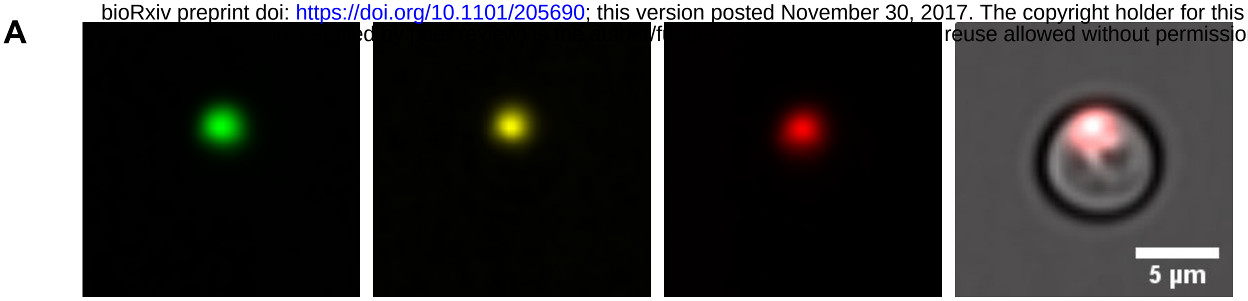
A
5 µm

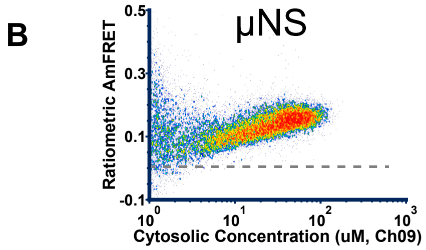
B
µNS
Ratiometric AmFRET
0.5
0.3
0.1
-0.1
10^0
10^1
10^2
10^3
Cytosolic Concentration (uM, Ch09)

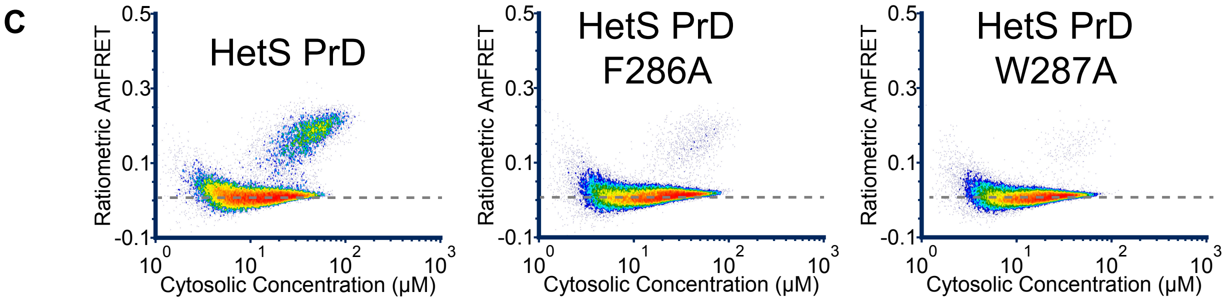
C
HetS PrD
HetS PrD F286A
HetS PrD W287A
Ratiometric AmFRET
0.5
0.3
0.1
-0.1
10^0
10^1
10^2
10^3
Cytosolic Concentration (µM)

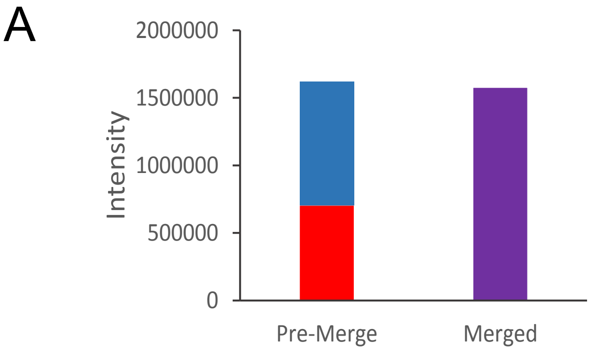
A
2000000
1500000
1000000
500000
0
Intensity
Pre-Merge
Merged

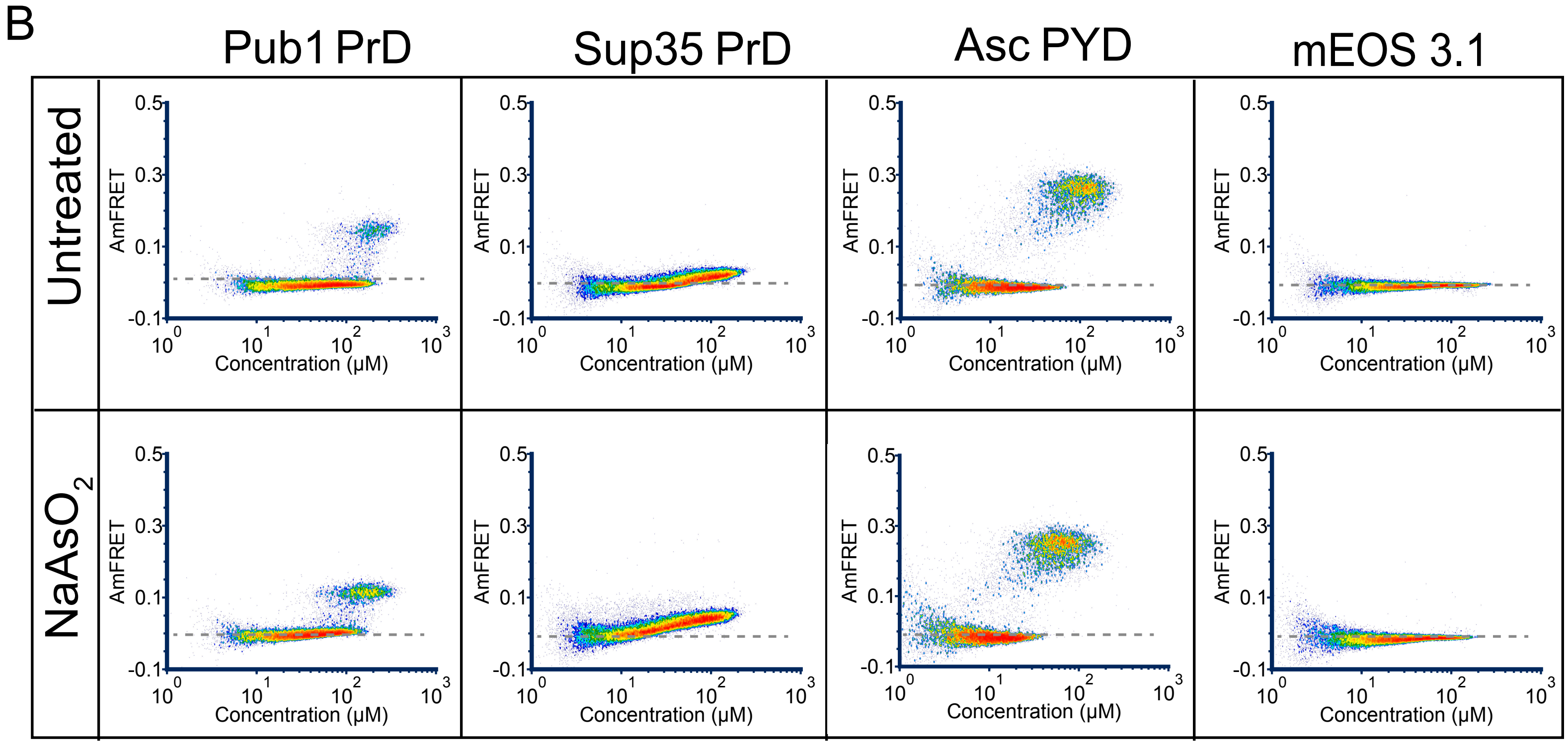
B
Pub1 PrD
Sup35 PrD
Asc PYD
mEOS 3.1
Untreated
$NaAsO_2$
AmFRET
0.5
0.3
0.1
-0.1
10^0
10^1
10^2
10^3
Concentration (μM)

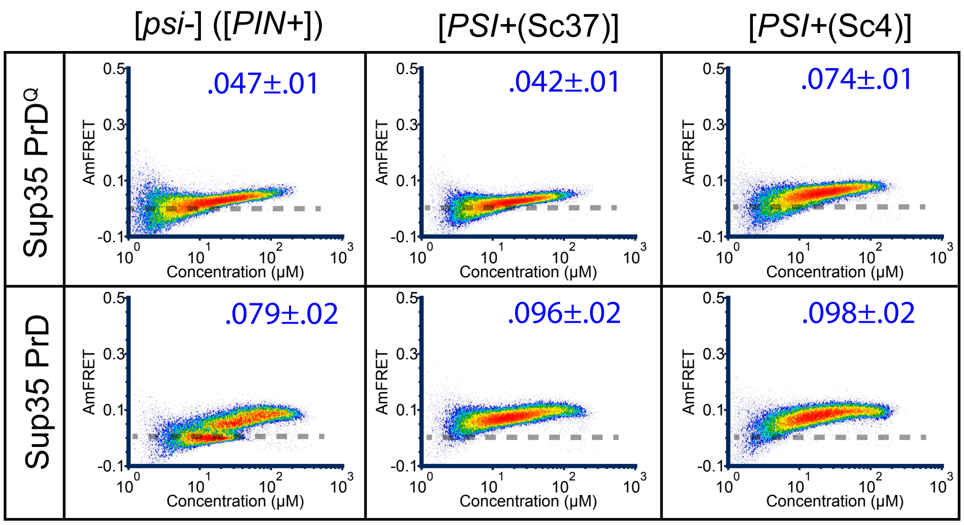
[psi-] ([PIN+])
[PSI+(Sc37)]
[PSI+(Sc4)]
Sup35 PrD^Q
Sup35 PrD
.047±.01
.042±.01
.074±.01
.079±.02
.096±.02
.098±.02
AmFRET
0.5
0.3
0.1
-0.1
10^0
10^1
10^2
10^3
Concentration (μM)